Episodic fluid flow in an active fault

Sarah Louis[1], Elco Luijendijk[1*], Istvan Dunkl[1], and Mark Person[2]

[1]University of Göttingen, Goldschmidtstrasse 3, 37077, Göttingen, Germany

[2] New Mexico Institute of Mining & Technology, 810 Leroy Place, MSEC 248, Socorro NM 87801 USA.

**Corresponding author, elco.luijendijk@geo.uni-goettingen.de*

ABSTRACT

We present a 250 ka record of episodic fluid flow along the Malpais fault which hosts the Beowawe hydrothermal system, Nevada, USA. The history of fluid flow was quantified using a novel combination of the apatite (U-Th)/He (AHe) thermochronometer and a model of the thermal effects of fluid flow. Samples show partial resetting of the AHe thermochronometer in a 40 m wide zone around the normal fault. Numerical models indicate that, using current fluid temperatures and discharge rates, fluid flow events lasting 2000 years or more lead to fully reset samples. Episodic fluid pulses lasting 1000 years result in partially reset samples, with 30 to 40 individual fluid pulses required to match the data. Episodic fluid flow is also supported by an overturned geothermal gradient in a borehole that crosses the fault, and by breaks in stable isotope trends in hydrothermal sinter deposits that coincide with two independently dated earthquakes in the last 20 ka. This suggests a system where fluid flow is triggered by repeated seismic activity and that seals itself over ~1000 years due to the formation of clays and silicates in the fault damage zone. Hydrothermal activity is younger than the 6-10 Ma age of the fault, which means that deep (~5 km) fluid flow was initiated only after a large part of the 230 m of fault offset had taken place.

INTRODUCTION

Fault hosted transient fluid flow and hydrothermal activity plays an important role in a wide range of geologic processes, including metalogenesis (Weis et al., 2012), oil migration (Boles et al., 2004), fault mechanics and metamorphism (Magee and Zoback, 1993). The timescale of fluid flow is important because the longer fluid flow is active, the more it changes subsurface temperatures and alters the rock matrix. Long-term changes in fluid flow and permeability in fault zones are driven by the competition between mineral precipitation (Lowell et al., 1993) and the creation of new flow paths by fault movement and the creation of connected fractures in fault damage zones (Sibson, 1981; Eichhubl et al., 2009). While field evidence of hydrothermal minerals precipitating in faults is common (Fisher et al., 2003; Eichhubl et al., 2009), data on changes of permeability or the duration of fluid flow in faults are rare, especially over geological timescales (10^4-10^7 years).

Determining the duration of fluid flow in hydrothermal systems is often difficult because not all hydrothermal systems generate mineral deposits that can be dated and because the uncertainty in dating hydrothermal minerals may exceed the duration of short hydrothermal events (Skinner, 1997). Several studies of fossil hydrothermal systems have demonstrated that low-temperature thermochronology offers new opportunities to date fluid flow by quantifying the thermal history of rocks in or adjacent to fluid conduits (Luijendijk, 2012; Gorynski et al., 2014; Hickey et al., 2014).

Here, we present a new approach to quantify the history of fluid flow in the active hydrothermal system of Beowawe in the Basin and Range Province, based on a combination of low-temperature thermochronology at high spatial resolution with a new model of conductive and advective heat flow. The results provide a novel record of episodic fluid flow activity in a normal fault over a timescale of ~250,000 years.

THE BEOWAWE HYDROTHERMAL SYSTEM

The Beowawe hydrothermal system is located in north-central Nevada, USA, southwest of the town of Elko (Fig. DR1). The area was the second most active geyser field in the USA after Yellowstone National Park. However, in 1960 geyser activity ceased due to geothermal development (White, 1998). The geysers and hot springs were located in the hanging wall of the Malpais fault, an active normal fault that formed when extension rotated to a northwest to southeast direction around 10 to 6 Ma (Zoback et al., 1981). The offset of the Malpais fault is approximately 230 m (Fig. DR1). Alluvial sediments along the fault document vertical offsets of 0.7 and 2 m caused by earthquakes at 18,700 and 7500 years BP, respectively (Wesnousky et al., 2005). Hydrothermal activity has generated an up to 65 m thick and 1600 m long sinter deposit, consisting predominantly of opal, at the footwall of the fault (Zoback, 1979). The sinter terrace is underlain by Middle Miocene volcanic rocks, including dacite, basaltic andesite and basalt, that overlie Ordovician sedimentary rocks (Struhsacker, 1980). Prior to 1960 the total fluid discharge was 0.018 m^3 sec^{-1}, of which one third discharged through the geysers and hot springs and two thirds contributed to lateral discharge through alluvial sediments (Olmsted and Rush, 1987). The low salinity of hydrothermal fluids and their stable isotope composition point to a meteoric origin. The system is recharged at a topographic high north-west of the geysers and is driven by both topography and thermal convection (Olmsted and Rush, 1987; Howald et al., 2015). Low $^3He/^4He$ ratios suggests that there is no magmatic heat source (Banerjee et al., 2011). Geothermometers and $\partial^{13}C$ concentration indicate that fluids were in contact with a carbonate reservoir at temperatures averaging 230°C at a depth of approximately 5 km (Rimstidt and Cole, 1983; Day, 1987; John et al., 2003).

METHODS

We collected seventeen surface rock samples of Middle Miocene pyroxene dacites along the Malpais fault in the vicinity of the Beowawe sinter terrace (Fig. 1). For four samples the crystallization age was dated using the zircon U-Pb method. The apatite (U-Th)/He thermochronometer (AHe) was used to constrain the post-formation thermal history. See Data Repository[1] section DR1.1-DR1.5 for description of the sampling and dating methods.

We used an advective and conductive heat flow model (Luijendijk, 2019) to simulate the thermal effects of upward fluid flux in a single fault zone and lateral flow into a connected alluvial aquifer. The model only simulates the discharge side of the hydrothermal system. Flow starts at 5 km depth in a carbonate formation that is the likely origin of upward flow. The flow rate is imposed and is based on the fluid budget of the Beowawe system (Olmsted and Rush, 1987). The temperature at the lower model boundary is fixed and based on measured regional geothermal gradients. We first quantified the timescale of the present-day (pre-1960) fluid flow system by calibrating fluid flow to a temperature record from well 85-18 (Iovenitti and Epperson, Jr., 1981) near the western edge of the sinter terrace (Fig. 1). We then ran models of continuous and episodic hydrothermal activity and compared modeled and measured AHe ages. Because hydrothermal activity may have varied temporally and spatially along the Malpais fault, the AHe samples were grouped along three profiles (Fig. DR1, Table DR1). For more details on the model setup see section DR1.6. in the Data Repository.

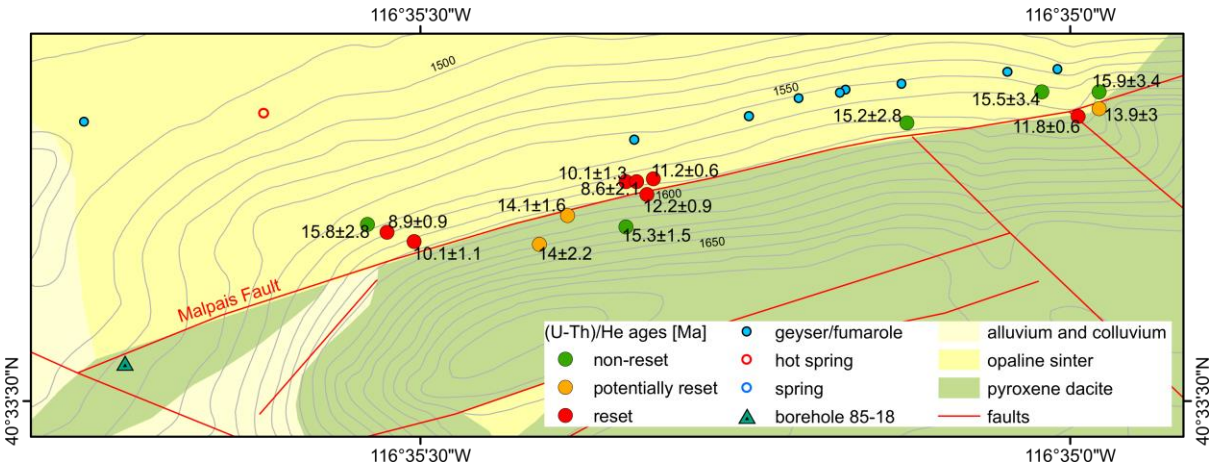

Figure 1 Geological map of the hydrothermally active Malpais fault, sample locations and measured AHe ages.

RESULTS

Short-lived fluid flow deduced from borehole temperatures

The temperature-depth profile in well 85-18 shows a bulge where the borehole crosses the Malpais fault at 550 m below the surface, with a small decrease in temperatures below the fault (Fig. 2G). The model results provide the best match to the observed temperature data for a fluid flow duration of 3000 years (Fig. 2). Longer runtimes would heat the system too much and would also not match the overturned geothermal gradient. Note that the model assumes constant flow rates over time. The duration may be less than 3000 years if one assumes that past flow rates and temperatures were higher than present rates due to a gradual decrease in permeability over time. In addition, a positive and negative inflection of the temperature profile can be observed above the Malpais fault at a depth of up to 500 m (Fig. 2G), which is caused by warm water flowing from the fault into alluvial sediments near the surface, and cool water flowing towards the fault through deeper permeable tuff or basalt layers (Olmsted and Rush, 1987).

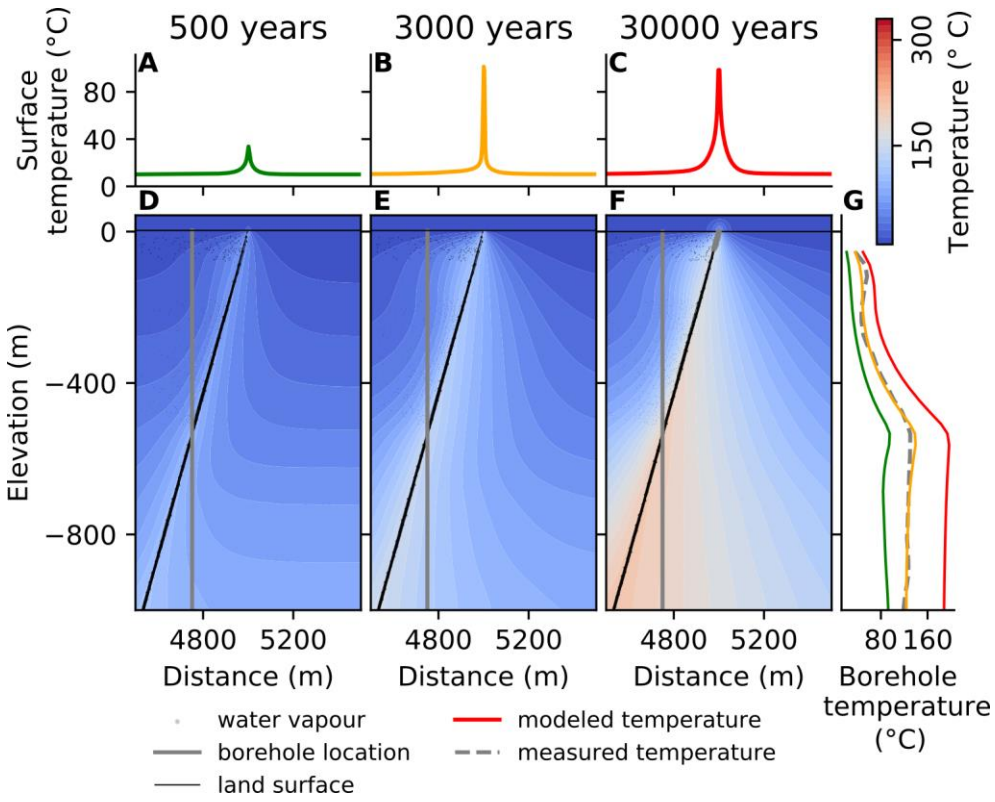

Figure 2 Comparison of modeled temperatures over time and borehole temperature record for borehole 85-18 indicates that fluid flow in this section of the fault is around 3000 years old (panel G). Panels A, B, and C show the surface temperature over time, panels D, E and F show the modeled temperature field and the location of the borehole. The measured borehole temperature data and the modeled temperatures for three time-slices are shown in panel G.

Long-term history of fluid flow using low-temperature thermochronology

The crystallization age of the volcanic host rock of the Beowawe hydrothermal system was dated using the zircon U-Pb method as 15.6 Ma. Samples at distances of more than 40 m from the Malpais fault show AHe ages that are equal to the U-Pb age (Fig. 1B), which signifies that they have not undergone heating of temperatures exceeding ~55-80°C since their deposition in the Miocene. In contrast, most samples that are close to the Malpais fault show a small but consistent decrease in AHe ages that is likely the result of heating by hydrothermal fluids (Fig. 1). The AHe data suggests that over long timescales hydrothermal activity was focused on the Malpais fault. However, while fluid flow originated in the fault, historically the surface discharge was focused on a line of geysers on top of the sinter terrace,

approximately 70 m north of the fault (Fig. 1B). The focus of hydrothermal activity on the Malpais fault is consistent with the location of the oldest generation of sinter deposits that have been found close to the fault (White, 1998).

We quantified the duration of hydrothermal activity by comparing a model of advective and conductive heat flow to measured AHe ages along three cross-sections perpendicular to the fault (Fig. 3E-H). We first modeled the effects of continuous hydrothermal activity. The best fit suggests that hydrothermal activity started about 70,000 years ago for profile B and C (Fig. 3E and DR10), and 90,000 years ago for profile A (Fig. DR9), which is shorter than the approximately 210,000 years that are required to deposit the volume of sinter at current fluid discharge rates and silica concentrations (Zoback, 1979). The results also indicate that the high fluid temperatures in the system would result in a full reset (AHe age=0 Ma) of the AHe thermochronometer in a 13 m wide zone around the fault bounded by a 5 m zone with partially reset samples after 70,000 years. For a duration of 200,000 years the width of the zone with fully reset AHe ages would be 45 m. However, even though the sampling was relatively dense, we did not find a single fully reset apatite (Fig. 1, Table DR6). This suggests hydrothermal activity was not continuous.

Model experiments of episodic hydrothermal activity show that periodic heating followed by thermal recovery results in only partially reset AHe ages around the fault and no fully reset samples (Fig. 3C). The best fit was obtained by 35 cycles of heating of 1000 years followed by 9000 years of thermal recovery (Fig. 3C). A model run with heating of 2000 years resulted in full resetting, whereas 500 years would not be sufficient to reduce AHe ages to their observed values (Fig. DR11). This suggests that the individual fluid pulses lasted longer than 500 but less than 2000 years. The duration of thermal recovery is not well constrained, any value of 6500 years or more provided a good fit. This means that the hydrothermal system must have been at least 255,000 years old. Analysis of the model error

(Fig. DR11) shows that the quantified duration of individual fluid pulses is relatively robust. However, the uncertainty of the total duration of fluid flow is affected by the uncertainty and dispersion of AHe ages and is estimated as ±80,000 years.

The modeled effects of hydrothermal activity on AHe ages are dependent on background exhumation rates, because land surface temperatures are buffered by air temperatures and exhumation rates need to be high enough to bring up rocks from deeper levels that have undergone sufficient heating. We assumed a background exhumation rate of 1×10^{-4} m a^{-1}, which is an average of reported regional values (see section DR1.8). Sensitivity analysis (Fig. DR8) shows that halving the exhumation rate would double the modeled duration of hydrothermal activity.

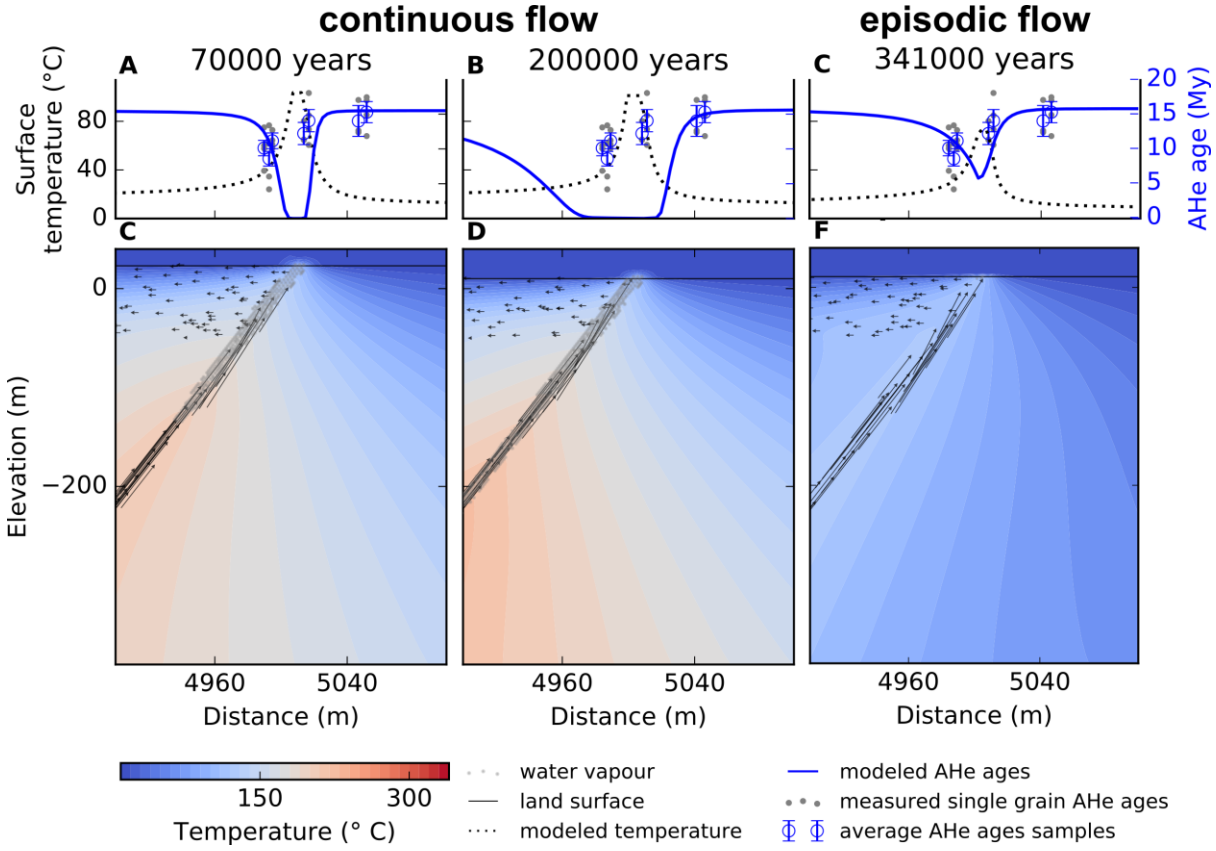

Figure 3 Modeled temperatures over long (ka) timescales around the Malpais fault and a comparison with measured AHe samples for continuous flow lasting 70,000 (A, D) and 200,000 years (B, E) and 35 cycles of episodic flow with 1000 years of fluid flow followed by 9000 years of thermal recovery (C, F). Panels A, C and E show a comparison between observed and modeled AHe ages for rocks at the surface. Panels B, D and F show modeled temperatures in a slice of the model domain around the Malpais fault.

DISCUSSION AND CONCLUSIONS

Episodic fluid flow

Two additional lines of evidence indicate that fluid flow in the Beowawe system occurred episodically over geological time scales. Variations in trace elements in sinter and salinities in fluid inclusions indicate changes in fluid sources over time (Leatherman, 2010). Carbon-14 ages and stable isotope data of sinter deposits show a change from a light to heavy $\delta^{18}O$ signature that coincides with an earthquake along the Malpais fault at 7500 years BP. The earthquake led to an increase in permeability, the opening of new flow paths and the incorporation of a new isotopically heavy fluid source that is in equilibrium with a 5 km deep carbonate formation (Howald et al., 2015). The much better fit of episodic fluid flow models to the AHe data (Fig. 3C) means that either fluid flow ceased in between the 1000 year-long fluid pulses, or that overall fluid flow in the Beowawe system was continuous but shifted location every ~1000 years. The last explanation is favored by the distribution of ^{14}C ages of hydrothermal sinter deposits (Howald et al., 2015) that suggests relatively constant fluid discharge over the last 20,000 years.

Relation between fluid flow and tectonic activity

The reconstructed duration of hydrothermal activity of ~250,000 years is much shorter than the 10 to 6 Ma duration of tectonic activity of the Malpais fault. One explanation for the relatively recent appearance of the Beowawe hydrothermal system may be that continuous fault movement has gradually increased permeability of the fault damage zone and permeability and fracture connectivity reached a threshold value that was sufficient to channel hydrothermal fluids along the fault from around 5 km depth around 250,000 years ago. The formation of connected pathways in the fault damage zone would have been slowed

by the extensive hydrothermal alteration around the fault, which has resulted in an clay-rich alteration zone with a low permeability (Cole and Ravinsky, 1984), and by the clogging of the fault zone with silica precipitated by hydrothermal fluids.

Although the stable isotope record by Howald et al. (2015) provides a clear indication of the effects of earthquakes on opening new flow paths, not all changes in fluid flow can be attributed to earthquakes. The temperature record of well 85-18 provides evidence for the opening of a new flow path along the Malpais fault around 3000 years ago (Fig. 2), whereas the latest earthquake was dated as 7500 BP (Wesnousky et al., 2005). In addition, the relocation of flow paths every 1000 years suggested by the thermochronological data exceeds the earthquake recurrence cycle. Our findings suggest that, in addition to earthquakes on the Malpais fault, new flow paths may be opened by permeability changes induced by earthquakes in nearby faults and the resulting changes in stress (Caskey and Wesnousky, 2000).

Quantifying fluid flow using low-temperature thermochronology

The combination of low-temperature thermochronology and numerical models of hydrothermal systems presented here potentially opens new avenues of research on the history of active hydrothermal systems. The method can be used where fluid temperatures are warm enough to affect the apatite (U-Th)/He thermochronometer (~55-80 ˚C, Reiners et al., 2005) and where exhumation rates are sufficient to bring up rocks from a depth of a few meters that have not been buffered by air temperatures. The method may be more suitable to date fluid flow in exhumed fossil hydrothermal systems, because the thermal footprint of fluid flow is much larger at depth. However, the advantage of studying an active hydrothermal system is that the fluid discharge and temperatures are known. For fossil hydrothermal systems there is a potential tradeoff between fluid temperatures and duration of

heating, with short heating at high temperatures providing the same thermal signal in adjacent rocks as long heating at lower temperatures. However, this could be remedied when fluid temperatures can be estimated independently from for instance fluid inclusion data. Alternatively, the use of multiple thermochronometers could provide constraints on timing because of their different sensitivities to heating time (Reiners, 2009).

ACKNOWLEDGMENTS

SL and EL gratefully acknowledge support by startup funding for postdocs grant number 3917542 by the University of Göttingen. Support to MP by the W.M. Keck foundation (989941) is gratefully acknowledged. The authors would also like to thank Volker Karius for the XRD measurements and Jonas Kley and David Hindle for helpful comments on an early version of the manuscript.

[1] GSA Data Repository item 201Xxxx, with description of the sampling, dating and modeling methods and additional model sensitivity analyses and model-data comparisons is available online at www.geosociety.org/pubs/ft20XX.htm, or on request from editing@geosociety.org or Documents Secretary, GSA, P.O. Box 9140, Boulder, CO 80301, USA.

REFERENCES CITED

Banerjee, A. et al., 2011, Deep permeable fault-controlled helium transport and limited mantle flux in two extensional geothermal systems in the Great Basin, United States: Geology, v. 39, p. 195–198, doi:10.1130/G31557.1.

Boles, J.R., Eichhubl, P., Garven, G., and Chen, J., 2004, Evolution of a hydrocarbon migration pathway along basin-bounding faults: Evidence from fault cement: AAPG

Bulletin, v. 88, p. 947–970.

Caskey, S.J., and Wesnousky, S.G., 2000, Active faulting and stress redistributions in the Dixie Valley, Beowawe and Bradys geothermal fields: implications for goethermal exploration in tha Basin and Range, *in* Twenty-Fifth Workshop on Geothermal Reservoir Engineering, Stanford, California, p. 1–16.

Cole, D.R., and Ravinsky, L.I., 1984, Hydrothermal alteration zoning in the Beowave geothermal system, Eureka and Lander Counties, Nevada.: Economic Geology, v. 79, p. 759–767, doi:10.2113/gsecongeo.79.4.759.

Day, G.A., 1987, Source of recharge to the Beowawe geothermal system north-central Nevada: University of Nevada Reno, 82 p.

Eichhubl, P., Davatz, N.C., and Becker, S.P., 2009, Structural and diagenetic control of fluid migration and cementation along the Moab fault, Utah: AAPG Bulletin, v. 93, p. 653–681, http://aapgbull.geoscienceworld.org/cgi/content/abstract/93/5/653.

Evans, K.F., 2005, Permeability creation and damage due to massive fluid injections into granite at 3.5 km at Soultz: 2. Critical stress and fracture strength: Journal of Geophysical Research B: Solid Earth, v. 110, p. 1–14, doi:10.1029/2004JB003169.

Fisher, Q.J., Casey, M., Harris, S.D., and Knipe, R.J., 2003, Fluid-flow properties of faults in sandstone: The importance of temperature history: Geology, v. 31, p. 965–968.

Gorynski, K.E., Walker, J.D., Stockli, D.F., and Sabin, A., 2014, Apatite (U-Th)/He thermochronometry as an innovative geothermal exploration tool: A case study from the southern Wassuk Range, Nevada: Journal of Volcanology and Geothermal Research, v. 270, p. 99–114, doi:10.1016/j.jvolgeores.2013.11.018.

Hickey, K.A., Barker, S.L.L., Dipple, G.M., Arehart, G.B., and Donelick, R.A., 2014, The brevity of hydrothermal fluid flow revealed by thermal halos around giant gold deposits: Implications for Carlin-type gold systems: Economic Geology, v. 109, p. 1461–1487,

doi:10.2113/econgeo.109.5.1461.

Howald, T. et al., 2015, Evidence for long timescale (>103 years) changes in hydrothermal activity induced by seismic events: Geofluids, v. 15, p. 252–268, doi:10.1111/gfl.12113.

Iovenitti, J.L., and Epperson, Jr., I.J., 1981, Beowawe Geothermal Area Evaluation Program - Final Report:, doi:10.2172/6509007.

John, D.A., Hofstra, A.H., Fleck, R.J., Brummer, J.E., and Saderholm, E.C., 2003, Geologic setting and genesis of the Mule Canyon low-sulfidation epithermal gold-silver deposit, north-central Nevada: Economic Geology, v. 98, p. 425–463.

Leatherman, M., 2010, Geochemistry and Reaction Path Modelling of the Beowawe Hydrothermal System, Nevada: A Barren End-Member Epithermal System [M.Sc. thesis]: University of Missouri-Columbia, 1-122 p.

Lowell, R.P., Van Cappellen, P., and Germanovich, L.N., 1993, Silica precipitation in fractures and the evolution of permeability in hydrothermal upflow zones: Science, v. 260, p. 192–194, doi:10.1126/science.260.5105.192.

Luijendijk, E., 2019, Beo v1.0: Numerical model of heat flow and low-temperature thermochronology in hydrothermal systems: Geoscientific Model Development Discussions, p. 1–17, doi:10.5194/gmd-2018-341.

Luijendijk, E., 2012, The role of fluid flow in the thermal history of sedimentary basins: Inferences from thermochronology and numerical modeling in the Roer Valley Graben, southern Netherlands [Ph.D. thesis]: Vrije Universiteit Amsterdam, 198 p.

Magee, M.E., and Zoback, M.D., 1993, Evidence for a weak interplate thrust fault along the northern Japan subduction zone and implications for the mechanics of thrust faulting and fluid expulsion: Geology, v. 21, p. 809–812, doi:10.1130/0091-7613(1993)021<0809:EFAWIT>2.3.CO;2.

Manga, M., Beresnev, I., Brodsky, E.E., Elkhoury, J.E., Elsworth, D., Ingebritsen, S.E.,

Mays, D.C., and Wang, C.Y., 2012, Changes in permeability caused by transient stresses: Field observations, experiments, and mechanisms: Reviews of Geophysics, v. 50, doi:10.1029/2011RG000382.

Olmsted, F.H., and Rush, F.E., 1987, Hydrogeologic reconnaissance of the beowawe geysers geothermal area, Nevada: Geothermics, v. 16, p. 27–46, doi:10.1016/0375-6505(87)90077-0.

Reiners, P.W., 2009, Nonmonotonic thermal histories and contrasting kinetics of multiple thermochronometers: Geochimica et Cosmochimica Acta, v. 73, p. 3612–3629, doi:10.1016/j.gca.2009.03.038.

Reiners, P.W., Ehlers, T.A., and Zeitler, P.K., 2005, Past, present, and future of thermochronology: Reviews in Mineralogy and Geochemistry, v. 58, p. 1.

Rimstidt, J.D., and Cole, D.R., 1983, Geothermal Mineralization I: The Mechanism of Formation of the Beowawe, Nevada, Siliceous Sinter Deposit.: American Journal of Science, v. 283, p. 861–875, doi:10.2475/ajs.283.8.861.

Sibson, R.H., 1981, Fluid Flow Accompanying Faulting: Field Evidence and Models, *in* Simpson, D.W. and Richards, P.G. eds., Earthquake Prediction, American Geophysical Union (AGU), p. 593–603, doi:10.1029/ME004p0593.

Skinner, B.J., 1997, Hydrothermal mineral deposits: what we do and don't know, *in* Barnes, H.L. ed., Geochemistry of hydrothermal ore deposits, John Wiley & Sons Inc.

Struhsacker, E.M., 1980, The Geology of the Beowawe Geothermal System, Eureka and Lander Counties, Nevada: University of Utah Research Institute, Earth Science Laboratory, p. 1–78.

Weis, P., Driesner, T., and A Heinrich, C., 2012, Porphyry-Copper Ore Shells Form at Stable Pressure-Temperature Fronts Within Dynamic Fluid Plumes: Science, v. 338, doi:10.1126/science.1225009.

Wesnousky, S.G., Barron, A.D., Briggs, R.W., Caskey, S.J., Kumar, S., and Owen, L., 2005, Paleoseismic transect across the northern Great Basin: Journal of Geophysical Research: Solid Earth, v. 110, p. 1–25, doi:10.1029/2004JB003283.

White, D.E., 1998, The Beowawe Geysers , Nevada , Before Geothermal Development: U.S. Geological Survey Bulletin, p. 1–28.

Ziagos, J.P., and Blackwell, D.D., 1986, A model for the transient temperature effects of horizontal fluid flow in geothermal systems: Journal of Volcanology and Geothermal Research, v. 27, p. 371–397.

Zoback, M.L.C., 1979, A geologic and geophysical investigation of the Beowawe Geothermal Area, North-Central Nevada: Stanford University Publications - Geological Sciences, v. 16.

Zoback, M.L.C., Anderson, R., and A. Thompson, G., 1981, Cainozoic Evolution of the State of Stress and Style of Tectonism of the Basin and Range Province of the Western United States: v. 300, 407-434 p., doi:10.1098/rsta.1981.0073.

Data Repository Item

Episodic fluid flow in an active fault

Sarah Louis[1], Elco Luijendijk[1*], Istvan Dunkl[1], and Mark Person[2]

[1]University of Göttingen, Goldschmidtstrasse 3, 37077, Göttingen, Germany

[2] New Mexico Institute of Mining & Technology, 810 Leroy Place, MSEC 248, Socorro NM 87801 USA·

**Corresponding author, elco.luijendijk@geo.uni-goettingen.de*

DR1: METHODS

DR1.1: Sampling and sample preparation

We collected seventeen surface rock samples of Middle Miocene pyroxene dacites along the Malpais fault in the vicinity of the Beowawe sinter terrace. All of them were taken at a different distance from the Malpais fault (Figure DR1, Table DR1). The samples were crushed and sieved. Apatite and zircon crystals were separated using a wet shaking table, dissolution of carbonates in 5% acetic acid, density separation using a lithium polytungstate solution and magnetic separation. Apatites and zircons were hand-picked from concentrates under an Olympus SZX7 microscope.

Table DR1 *Locations of samples and their distance to the Malpais fault.*

Sample ID	Latitude (WGS84)	Longitude (WGS84)	Distance to Fault (m)	Cross-section
B1	-116.59235	40.560600	56 N	A
B2	-116.59210	40.560500	40 N	A
B3	-116.59175	40.560384	15 N	A
B4	-116.59018	40.561134	48 N	No data
B5	-116.58978	40.560717	7 S	B
B6	-116.58370	40.562300	35 N	C
B7	-116.58543	40.561900	18 N	C
B8	-116.58903	40.561150	20 N	B
B9	-116.58890	40.561150	17 N	B
B10	-116.58868	40.561184	15 N	B
B11	-116.58323	40.561984	10 S	C
B12	-116.58296	40.562084	8 S	C

B13	-116.58876	40.560984	4 S	B
B14	-116.58903	40.560567	42 S	B
B15	-116.59014	40.560344	37 S	B
B16	-116.58296	40.562300	19 N	C
B17	-116.59615	40.561134	242 N	Discarded

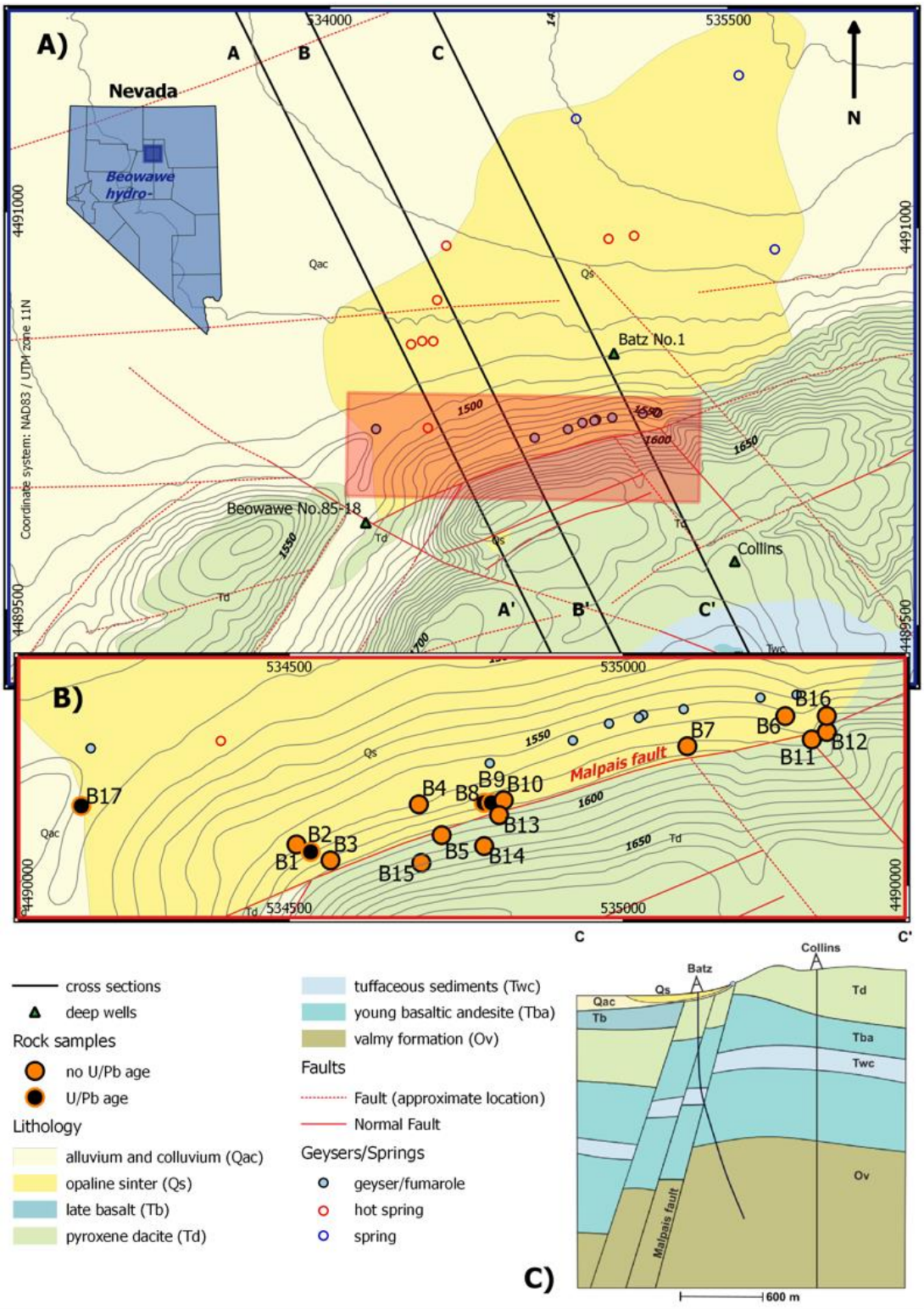

Figure DR1 *Panel A) shows the local geological setting, locations of wells, the three different cross-sections A-A´, B-B´ and C-C' and the location of the geysers and hot springs. Panel B) is a close-up of the hydrothermally active Malpais fault and shows the location of the rock samples that were used for zircon U-Pb dating and apatite (U-Th)/He analysis. Panel C) depicts the cross-section C-C' of the Beowawe geothermal area.*

DR1.2: Zircon U-Pb geochronology

The hand-picked zircon crystals from samples B-2, B-8, B-9 and B-17 were fixed on a double-side adhesive tape attached to a thick glass plate and embedded in a 25 mm diameter epoxy mount. The crystal mounts were lapped by 2500 mesh SiC paper and polished by 9, 3 and 1 µm diamond suspensions. For all zircon samples and standards used in this study cathodoluminescence (CL) images were obtained using a JEOL JXA 8900 electron microprobe to study their internal structure and to select homogeneous parts for the in-situ age determinations. The carbon coating used for CL imaging was later removed with a brief hand polish on a 1 µm diamond cloth. The in-situ U-Pb dating was performed by laser-ablation single-collector sector-field inductively coupled plasma mass spectrometry. The method employed for analysis is described in detail by Frei & Gerdes (Frei and Gerdes, 2009). A Thermo Element 2 mass spectrometer coupled to a Resonetics Excimer laser ablation system was used. All age data presented here were obtained by single spot analyses with a laser beam diameter of 33 µm and a crater depth of approximately 10 µm. The laser was fired at a repetition rate of 5 Hz and at nominal laser energy output of 25 %. Two laser pulses were used for pre-ablation. The carrier gases were He and Ar. Analytes of ^{238}U, ^{235}U, ^{232}Th, ^{208}Pb, ^{207}Pb, ^{206}Pb, mass 204 and ^{202}Hg were measured by the ICP-MS. The data reduction is based on the processing of ca. 50 selected time slices (corresponding ca. 14 seconds) starting ca. 3 sec. after the beginning of the signal. The age calculation and quality control are based on the drift- and fractionation correction by standard-sample bracketing using GJ-1 zircon reference material (Jackson et al., 2004). For further control the Plešovice zircon (Sláma et al., 2008), the 91500 zircon (Wiedenbeck et al., 1995) and the FC-1 zircon were analyzed as "secondary standards". The age results of the standards were consistently within 2σ of the published ID-TIMS values. Drift- and fractionation corrections and data reductions were performed by our in-house software (UranOS; (Dunkl et al., 2008)). The level of Hg-corrected ^{204}Pb signal was very low, thus no common lead correction was required. The number of single-grain ages per sample ranges between 20 and 47. Concordia plots (Figure DR7) were constructed by the help of Isoplot/Ex 3.0 (Ludwig, 2012).

The dated zircon crystals have significantly lower radiation damage density, than the zircon reference materials used for correction of the fractionation (1.7×10^{16} in the samples and 6.1, 7.4 and 3.1×10^{17} alpha decay/g in the GJ1, Plešovice and 91500 zircons, respectively). The increasing radiation damage density has an impact on the ablation rate of zircons (Marillo-Sialer et al., 2014) and it needs a correction that is based on the offset between the TIMS ages

and laser ablation ages detected on a series of reference material having different degree of metamictization (Sliwinski et al., 2017). These RDC (radiation damage corrected) ages can be considered as the most reliable approximation of the crystallization age of zircons.

DR1.3: Apatite (U-Th)/He thermochronology

Apatite crystals were hand-picked under a binocular microscope. Selected crystals had a minimum width of 60 µm, euhedral shape and equal widths in all directions perpendicular to the c-axis. To secure intact shape and exclude minerals with inclusions and cracks, further selection was done using a polarizing microscope. Four apatite crystals per sample were analyzed. The mineral grains were enclosed in a pre-cleaned platinum capsule of ~1x1 mm size. The Pt capsules were heated in the full-metal extraction line by an infra-red laser for 2 minutes in high vacuum. The extracted gas was purified using a SAES Ti-Zr getter while being kept at 450°C. The chemically inert noble gases and a minor amount of other rest gases were then expanded into a Hiden triple-filter quadrupole mass spectrometer equipped with a positive ion counting detector. Beyond the detection of helium, the partial pressures of some rest gases were continuously monitored (H_2, CH_4, H_2O, N_2, Ar and CO_2). Crystals were checked for degassing of He by sequential reheating and He measurement. The amount of He extracted in the second runs are usually below 1%. Following degassing, samples were retrieved from the gas extraction line, spiked with calibrated ^{230}Th and ^{233}U solutions. The apatite crystals were dissolved in a 4% HNO_3 + 0.05% HF acid mixture in Savillex teflon vials. Spiked solutions were analyzed by isotope dilution method using a Perkin Elmer Elan DRC II ICP-MS. The (U-Th)/He ages were calculated by the Taylor Expansion Method (Braun et al., 2006). (U-Th)/He ages were corrected for alpha ejection (F_T correction) (Farley, 2000).

DR1.4: Determination of internal zoning of actinide elements in the apatite crystals

The correction of alpha ejection assumes homogeneous distribution of alpha-emitting elements within the dated crystals. Zonation of U and Th would affect the correction of alpha ejection, resulting underestimation or overestimation of ages (Meesters and Dunai, 2002a). To describe the internal distribution of actinide elements in the apatite samples we performed laser ablation trace element determination along lines across polished half-crystals perpendicular to the c-axis. Laser ablation cross profiling was performed with a 10 µm beam diameter, with a speed of 3 µm s^{-1}.

DR1.5: Quantitative sample analysis using XRD and Rietveld method

To determine the rock composition and look for secondary minerals we conducted x-ray diffraction (XRD) on five samples (B-4, B-5, B-8, B-9, B-14) using a Philips X'Pert MPD and a PW 3050/10 goniometer. The sieved sample fraction <250µm was mixed with the internal standard zinc oxide (ZnO) at a ratio of 8/2 respectively. The mixture was then back loaded on a powder mount with a diameter of 27mm. Measurement settings are summed up in the table below (Table DR2). The diffractogram was analyzed qualitatively using the software X'pert High Score by PANAlytical. Qualitative analysis was performed with the Rietveld method (Young, 1995).

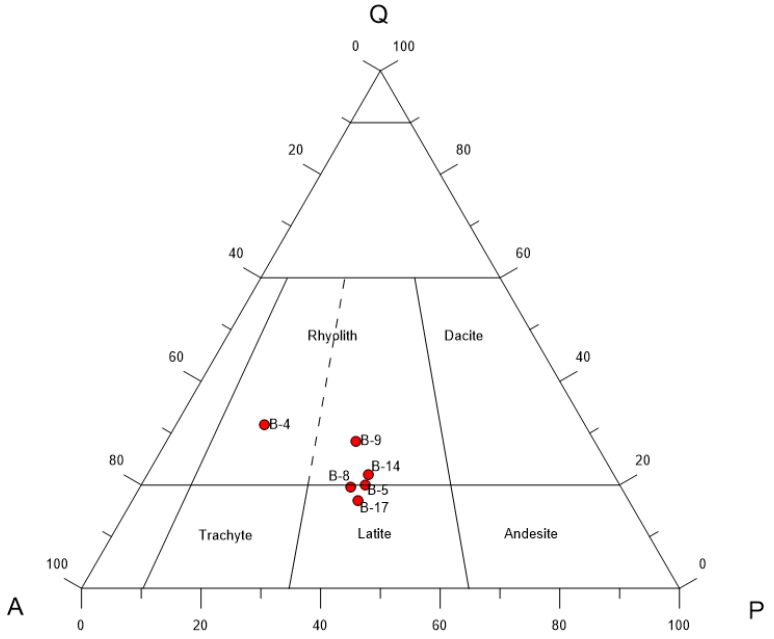

Figure DR2 *Streckeisen diagram showing the total weight percentage of all quartz, potassium feldspar and plagioclase mineral phases in the analyzed samples.*

The crystal phases of all six samples were determined using the Rietveld method (after Young (1995)). The total weight percentage of all quartz, potassium feldspar and plagioclase mineral phases were added up respectively and normalized to 100%. Results were plotted into a Streckeisen diagram (Figure DR2, Table DR2 and DR7). Contradicting the geological map of Stuhsacker, the majority of samples plotted into the lower rhyolite field of the Streckeisen diagram. Sample B-17 contains less Quartz and its zircons contain more U and Th than most other samples. It plots into the latite field.

Table DR2 *XRD settings*

Anode material of x-ray tube	Copper (Cu)
Voltage	40 kV
Current	30 mA
Mask	17.20 mm
Divergent slit angle	0.5°
Distance of divergent slit to sample	140 mm
Anti-scatter slit angle	0.5°
Height of receiving slit	0.2 mm
Scan range	4.0° – 69.5°
Step size	0.02°
Counting time	10 sec

DR1.6: Thermal model

We used a new inverse 2D thermal model code, Beo, to simulate the temperature history of the rocks surrounding a hydrothermal system. See Luijendijk (2019) for more details on the model code. Beo is an open source code and is available at https://github.com/ElcoLuijendijk/beo.

The model code simulates advective and conductive heat transfer and uses the modeled temperature history to model apatite (U-Th)/He ages of synthetic rocks samples. Beo uses the generic finite element code Escript (Gross et al., 2007b, 2007a; Poulet et al., 2012) to solve the heat advection and conduction equation. The model setup and boundary conditions are shown in Figure DR3. The fluid flux term (q) is a fixed value in a single fault zone and one or two horizontal aquifers connected to this fault. A fixed temperature is assigned to the lower model boundary that is based on the regional geothermal gradient. No heat flow is allowed over the left and right hand model boundary. The upper model boundary consists of a layer of 10 m of air overlying the land surface. The top boundary is assigned a specified temperature that corresponds to the average annual air temperature of 10˚C. Heat transfer between the surface and the atmosphere is modeled as conductive heat flow. A variable and artificially high value of thermal conductivity of the air layer is calculated following equations for sensible and latent heat flow by Bateni and Entekhabi (Bateni and Entekhabi, 2012) to account for the relatively efficient heat transport at the land surface. The reason for using this boundary condition is that it provides a physically realistic heat flux at the land surface, and it avoids applying a fixed temperature or heat flux, which would skew

the model results because both temperature and heat flux at the surface vary over time. The thermal conductivity in the subsurface was dependent on lithology. The model does not take into account the presence of an unsaturated zone away from the hot spring area, where thermal conductivities may be lower than below the water table.

Apatite (U-Th)/He ages were calculated using the modeled thermal history following a helium diffusion model by Meesters and Dunai (2002b, 2002a), with helium diffusivity calculated as a result of radiation damage following the RDAAM model (Flowers et al., 2009). Modeled AHe ages were compared with measured ages on a single grain basis. The ages were calculated using the grain radius and U, Th and Sm content of each grain as input data. For visual reference the model also calculates the AHe age for each point at the land surface using the average apatite properties of all samples that are included in a particular model run. The misfit of the model was quantified by calculating the mean error and the mean absolute error of the modeled and measured single grain AHe ages.

In this study, the thermal history was calculated for three cross-sections perpendicular to the Malpais fault (A-A', B-B' and C-C', Figure DR1). The samples closest to either cross section were projected onto each section. The three cross sections were chosen because the thermal conditions vary along strike along the sinter terrace, as evidenced by different borehole temperatures at the western and eastern part of the sinter terrace (Garg et al., 2007). In addition, hydrothermal activity may have shifted its locus over time (Leatherman, 2010), which may result in different temperature histories and AHe data for each cross-section. Profile length and width of the model domain are 8000 m and 2000 m respectively. The model contains a single normal fault, the Malpais fault. The subsurface consists of different lithologies that show an offset between the hanging wall and the foot wall of the Malpais fault. For our model setup we chose the lithology of the deep well Collins 76-17 (Sibbett, 1983). According to Zoback (Zoback, 1979), the net offset between the top of the volcanic sequence of the Malpais rim and the subsidiary block is 230 m. Grid size varied between 250 m for the grid cells away from the fault zone, 2 m for the cell size in the air layer, 2.5 m within the fault damage zone and 500 m at the model base.

The fixed parameters for the thermal model were taken from previous studies on the Beowawe system. The geology was based on a profile by Hoang et al. (Hoang et al., 1987) and information from deep wells (Chevron Resource Company, 1979) (Figure DR3). Bulk thermal conductivities of volcanic and intrusive rocks were determined at ~2 W m^{-1} K^{-1} with exceptions of significantly lower conductivities for basalt and tuffaceous sediments, which were assigned a thermal conductivity of 1.6 and 1.33 – 1.65 W m^{-1} K^{-1}, respectively (Smith,

1983). Modeled present-day temperatures were compared with borehole temperatures recorded by Iovenitti And Epperson, Jr. (Iovenitti and Epperson, Jr., 1981) in borehole 85-18 that is located at 250 m NW of the Malpais fault (Figure 1).

The modeled fluid fluxes were based on a previously published groundwater budget of the area (Olmsted and Rush, 1987). The total fluid flux of the hydrothermal system is 380 m^2 a^{-1}. Deflections in the temperature-depth profile of wells Beowawe 85-18 suggests that lateral flow occurs at low depth. According to Olmsted and Rush (Olmsted and Rush, 1987) the up to 50 m thick quaternary alluvium that underlies the sinter terrace and extends into the valley channels 2/3 of the total fluid flux from the Malpais fault towards the valley. The remaining 1/3 of the fluid flux is discharged as spring flow near the fault. All variable parameters are set to their base values as described in Table DR3 and Table DR4.

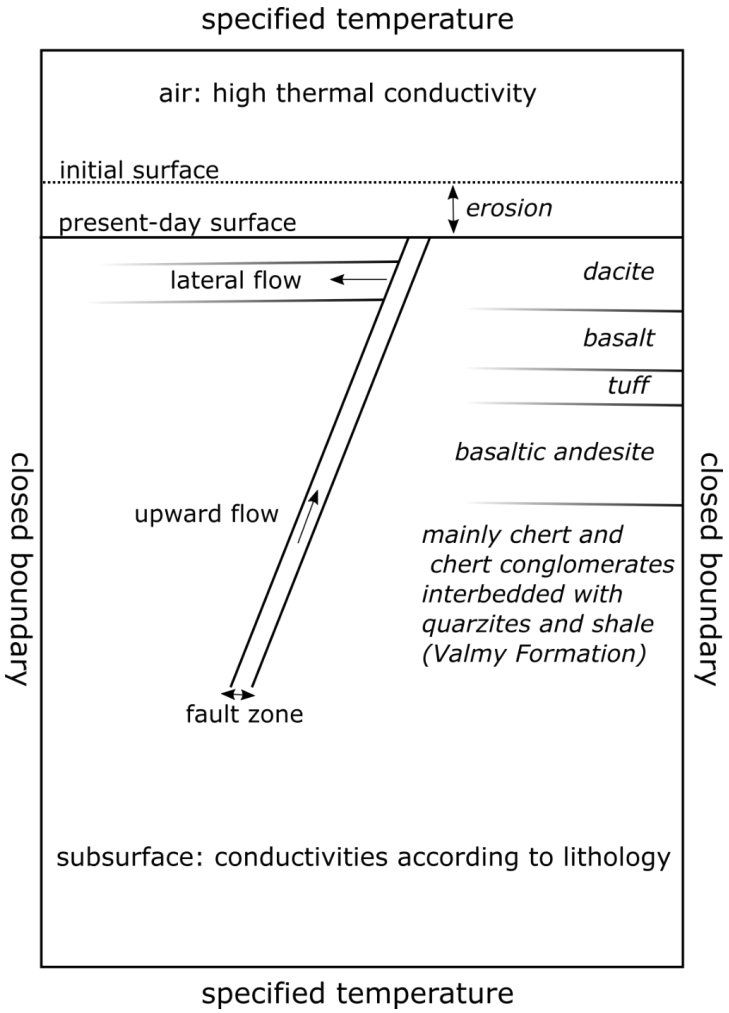

Figure DR3 *Schematic diagram depicting the hydrostratigraphic framework model of the discharge area of the Beowawe hydrothermal system. The upper and lower boundary conditions were assigned a specified temperature according to the average annual air*

temperature and the regional geothermal gradient. No heat flow is allowed over the left and right hand model boundary. Fluid flows upwards along a single fault zone, part of the flux contributes to lateral flow in one or more aquifers that are connected to the fault. The remaining fluid discharges at the surface. The bottom of the fault is located above the lower boundary of the model domain to avoid interference of the boundary with modeled fluid temperatures. Heat transfer between the surface and the atmosphere is modeled as a conductive heat flow. Heat transfer in the subsurface is determined by the specific thermal conductivities of the local lithologies. The land surface is lowered in steps of 1 m to account for erosion over longer timescales.

DR1.7: Borehole temperature data

We compared modeled temperatures with borehole temperature data from hydrothermal exploration programs from the deep well Beowawe 85-18 (Figure 2). Beowawe 85-18 was drilled and completed from February 22nd 1980 to June 2nd 1980. Temperature-depth profiles were conducted in five separate runs on May 10th and 11th 1980 (Iovenitti and Epperson, Jr., 1981).

DR1.8: Model sensitivity analysis

A sensitivity analysis was performed to test the influence of model parameters on the thermal overprint of AHe data in surface samples adjacent to the hydrothermally active Malpais fault. The parameters and their ranges are listed in Table DR3. A first model run was performed with the initial base values that were taken from earlier studies on the Beowawe hydrothermal system. For each parameter listed in Table DR3, a range of values were tested by changing the parameter in each model run while keeping all other parameters fixed to their initial base values.

No direct measurements of the Malpais damage zone width were performed. However, studies on fault zone architecture show that there is a positive correlation between fault damage zone (or fault thickness) and displacement (Caine et al., 1996; Childs et al., 2009; Bense et al., 2013). Based on these studies we derived an estimate of the fault damage zone for the Malpais fault. With a displacement of ~230 m and a crystalline bed rock we used fault zone thickness values varying between 10 and 30 m for our parameter range (Table DR3).

We used a background geothermal gradient of 0.04°C m^{-1} (Howald et al., 2016). This is in accordance with Zoback's (Zoback, 1979) reported reservoir temperature of 210-230°C. The deep reservoir is located in a carbonate layer of the Valmy Formation at depth of ~5 km. Smith (Smith, 1983) reports a general background heat flow of 110 mW m^{-2} in this part of the Battle Mountain heat flow high. With thermal conductivities varying between 1.6 and 4.4 W m^{-1} K^{-1} for the different lithologies, the geothermal gradient could vary between 0.02 and 0.07°C m^{-1}.

The exhumation rate was varied between 1×10^{-3} and 7.5×10^{-5} m a^{-1}. Estimates of erosion and exhumation rates in the Basin and Range vary widely. Low temperature thermochronology indicates long-term (millions of years) exhumation rate of 6 x 10^{-4} m a^{-1} for the Wassuk range in the eastern part of the Basin and Range (Stockli et al., 2002). Surface exposure dating using cosmogenic nuclides suggests relatively high short-term erosion rates of 5 x 10^{-3} m a^{-1} in the Yucca mountains (Gosse et al., 1995). In contrast, a cosmogenic nuclide study in SE-Arizona by Jungers & Heimsath (2016) suggested much lower erosion rates of 3 x 10^{-5} to 6 x 10^{-5} m a^{-1}. In the Sierra Nevada, west of the Basin and Range, exhumation varies between 1 x 10^{-5} to 3 x 10^{-4} m a^{-1}, with a strong correlation of the rate of exhumation and the proximity to active faults (Riebe et al., 2000). Given the high activity of the Malpais fault as shown by the prominent fault scarp and two dated earthquakes over the last 20,000 years (Wesnousky et al., 2005) we adopt a exhumation rate of 1 x 10^{-4} m a^{-1} over the last 500,000 years as a base case. Given the large uncertainty of this value we explore a wide range of exhumation rates using sensitivity analysis. We also tested the effects of relatively high exhumation rates of 1×10^{-3} m a^{-1} that reflect rates in active mountain belts (Herman et al., 2013).

Based on a detailed study on the hydrogeology of the Beowawe geothermal system by Olmsted and Rush (1987), the pre-developmental discharge rate at the Beowawe hydrothermal system was estimated to have been ~380 m^2 a^{-1}. This value is based on recent hydrogeological activity. However, this value may have changed over geological timescales. Nolan and Anderson (1934) reported that hydrothermal discharge varied seasonally, indicated by more energetic activity during the winter months. Both Howald et al. (2015) and Banerjee et al. (2011) suggest a transient and episodic fluid flow for the Beowawe system, with changes over a timescale of approximately 7000 years. To quantify the effect of changing fluid fluxes we included values ranging between 100 and 600 m^2 a^{-1} in the sensitivity analysis.

Table DR3 *Parameters used for modeling and ranges of values tested in sensitivity analysis.*

Parameter	**Base Value**	**Range**	**Unit**
Exhumation rate	0.0001	1×10^{-3} - 7.5×10^{-5}	M a^{-1}
Geothermal gradient	0.04	0.02 - 0.07	C° m^{-1}
Fault width	10	10 – 40	m
Fault flux	400	100 – 600	m^2 a^{-1}
Width of model domain	2000		m
Depth of model domain	8000		m
Cell size	250		m
Cell size air layer	10		m
Cell size fault zone	2.5		m
Cell size at land surface	100		m
Cell size base	500		m
Fault angle	65		°
Fault bottom	5000		m BGS
Air temperature	10		°C
Aerodynamic resistance	80	20 - 140	s m^{-1}
Crystallization age host rock	15.7		Ma
Stopping distance of alpha particle	2.10×10^{-5}		m

Table DR4 *Depth and properties of the different lithologies. The depth of lithologies of the footwall taken from deep well Collins* (Sibbett, 1983), *thermal conductivity was based on Smith* (Smith, 1983) *and porosity on Freeze and Cherry* (Freeze and Cherry, 1979).

Lithology	**Bottom of layer (footwall) (m BGS)**	**Porosity (dimensionless)**	**Thermal conductivity (W m^{-1} K^{-1})**
dacite	370	0.08	2
basalt	550	0.05	1.6
tuff	720	0.2	1.58
basaltic andesite	950	0.05	2.26
Valmy formation		0.05	4.44

DR2: RESULTS

DR2.1: U-Pb geochronology

The average zircon U-Pb age of four dacite samples was determined to be 15.6 Ma (Table DR5, Fig. DR7), which is slightly younger than previously reported K-Ar ages of the same volcanic unit (Struhsacker, 1980).

Table DR5 *Results of U-Pb analysis. Ages are shown in Ma including their decay constant errors. For samples B-2, B-8 and B-9 a total of 15 crystals were analyzed and for samples B-17 17 crystals were analyzed. Unc. is uncertainty, prob. denotes probability and corr. denotes corrected.*

Sample	Dated crystals	N crystals	Concordia age (Ma)	Unc. (Ma)	MSWD	Prob.	U ($\mu g\ g^{-1}$)	Th ($\mu g\ g^{-1}$)	Log alpha Density $(alpha/g)^{-1}$	Corr. Age (Ma)	Unc. (Ma)
B-2	15	13	15.25	0.11	0.07	0.79	1358	1985	16.9	15.6	0.3
B-8	15	14	15.23	0.10	0.18	0.68	1283	1329	16.9	15.6	0.3
B-9	15	15	15.02	0.11	2.80	0.10	1253	1057	16.9	15.4	0.3
B-17	17	17	15.47	0.05	0.01	0.91	1959	3231	17.1	15.7	0.3

DR2.2: Apatite (U-Th)/He data

Table DR6 summarizes the results of (U-Th)/He analysis. The map in Figure DR1 shows the surface samples along the Malpais fault, and figure DR4 shows the single grain ages and the distance to the Malpais fault for the three profiles.

Single grains that are significantly out of line with the others were excluded from the analysis (marked grey in Table DR6). These outliers can be the result of tiny inclusions or zoning in the actinide content of the dated apatite crystal. Sample B4 did not yield enough suitable apatites and was omitted.

The unweighted average age of six samples (B-1, B-6, B-7, B-14, B-16) show AHe ages similar to the U-Pb age of the host rock. These samples have not experienced detectable thermal overprint since their crystallization. Most of them are located at distances of approximately 50 m away from the main fault. Samples B-16 and B-7 are located at distances of ~15 m to ~20 m to the fault respectively. Two samples are potentially partially reset (B-5 and B-12), which means that these samples have a younger AHe age than the crystallization age but their uncertainty is in the range of the U-Pb age. Both are within a distance of about

10 m from the Malpais fault. The remaining 7 samples are younger than the emplacement age, showing a thermal overprint on their AHe age (B-2, B-3, B-8, B-9, B-10, B-11, B-13). These samples are within a distance of only a few m to up to ~40 m from the hydrothermally active normal fault.

The sample that is furthest away from the fault (B-17) does appear to be an outlier with an AHe age averaging 23.3 Ma. This is significantly higher than the U-Pb age of zircons in the same sample. However, the AHe ages themselves are robust analytically: AHe ages for the Durango standard that were included in the same batch and did match the age of the standard with an error of 2.3 %. We checked if the anomalously old ages could be caused by zonation and measured the actinide distribution in the sample. The grains do not exhibit a strong zonation. However, the grain quality was suboptimal. All the apatite grains that we found for this sample had small solid and fluid inclusions. This is the most likely cause for the anomalous AHe ages. Given the poor sample quality we now decided to take sample B17 out of the main manuscript and omitted it in our models**.**

To assess the impact of zonation of alpha-emitting element in the apatite crystals on the measured AHe ages, the actinide concentrations in single crystals were imaged using laser ablation (Fig. DR6). The laser ablation line measurement has shown variable patterns in actinide concentration, with both core and rim-zoned crystals for a number of 24 grains from 7 samples (B-1, B-2, B-5, B-7, B-8, B-9, B-13). For most grains the actinide concentration is about 15% in the outer most 10 µm. Following the He-diffusion model HeFTy (Ketcham, 2005), the difference in modeled ages between the homogeneous assumption and rim zoned grains is approximately 100 to 200 ka for typical grain properties found in this study (radius: 70 µm, U: 6 ppm, Th: 17 ppm, Sm: 370 ppm). Given the relatively small magnitude of the error induced by zonation, we assumed homogeneous U-Th-Sm distributions for calculating AHe ages using alpha ejection (F_T) correction and all further model-data comparison.

The dispersion of the single grain ages is relatively high and in many cases the difference between AHe ages of apatite grains in single samples exceed the analytical errors of these samples. The single grain AHe ages do not exhibit any correlation with effective uranium (eU) content as shown in Fig. DR5. Overall the apatites exhibit relatively low eU values, with all but one samples (B16) showing values that are below typical eU values of 28 ppm (Flowers et al., 2009). Given the young crystallization age of the apatites of 15.6 Ma and the low eU content the effects of radiation damage on AHe diffusivity and AHe ages is probably small and is not a likely explanation for the dispersion in single grain ages that is observed in the samples.

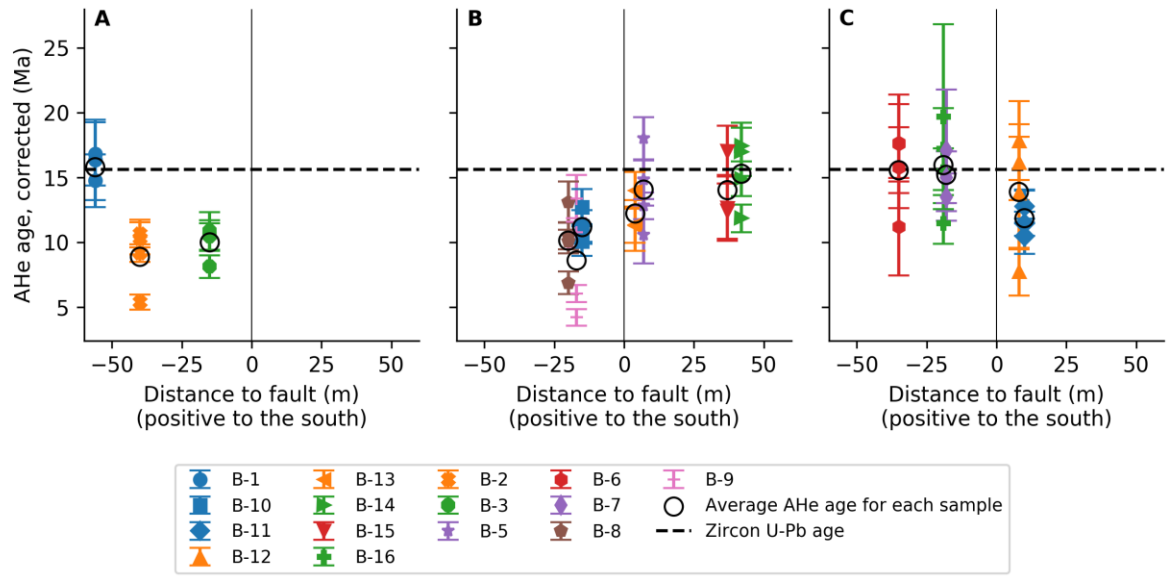

Figure DR4 *Measured AHe single grain ages and average sample ages for the three profiles A, B and C. The error bars denote plus or minus 2 SE.*

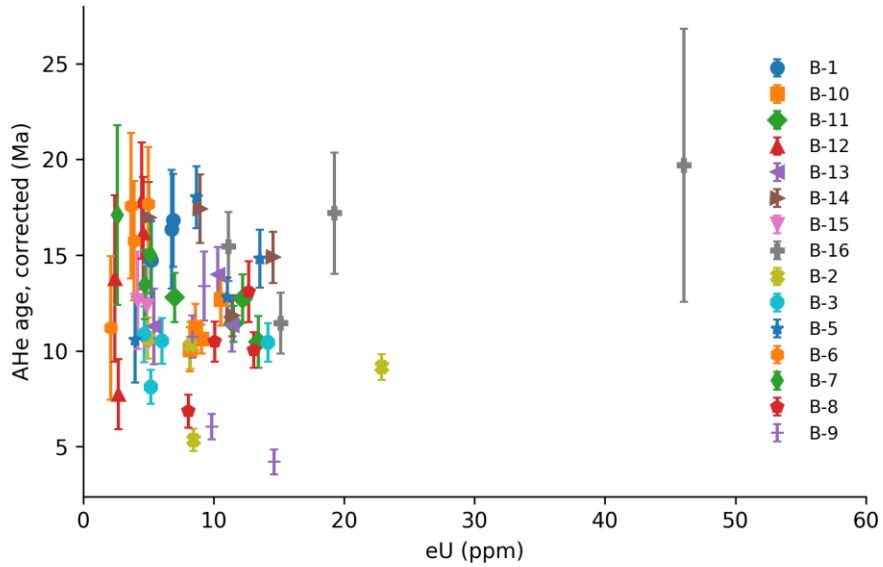

Figure DR5 *Relation between AHe single grain ages and effective uranium (eU) content. There is no statistical significant relation between AHe age and eU. Most of the apatites in our dataset have a relatively low eU value, at which significant effects of radiation damage on AHe ages would not be expected following data and models by Flowers et al.* (2009).

Table DR6 *Results of apatite (U-Th)/He analysis.*

		He		U			Th				Sm			Ejection	*Uncorr.*	Ft-Corr.		Sample unweighted aver. ± 1 s.e.	
Sample	Sphere radius [μm]	vol. [ncc]	1σ [%]	mass [ng]	1σ [%]	conc. [ppm]	mass [ng]	1σ [%]	conc. [ppm]	Th/U ratio	mass [ng]	1σ [%]	conc. [ppm]	correct. (Ft)	*He-age [Ma]*	He-age [Ma]	2σ [+/- Ma]	[Ma]	[Ma]
B-1 a1	39.5	**0.0180**	4.5	**0.0057**	14.0	3.5	**0.0224**	3.0	13.7	3.92	**0.550**	8.4	336	**0.587**	*9.59*	**16.34**	3.10		
B-1 a2	40.9	**0.0229**	4.1	**0.0051**	17.8	1.5	**0.0150**	3.2	4.3	2.92	**0.511**	8.4	147	**0.594**	*14.72*	**24.77**	5.17		
B-1 a3	52.7	**0.0301**	3.4	**0.0088**	9.3	4.0	**0.0275**	2.9	12.3	3.12	**0.731**	8.3	328	**0.695**	*11.68*	**16.82**	2.43		
B-1 a4	56.7	**0.0320**	3.4	**0.0102**	8.2	3.0	**0.0302**	2.8	9.0	2.98	**0.945**	8.3	283	**0.716**	*10.55*	**14.75**	2.03	**15.78**	2.23
B-1 a5	68.6	**0.1265**	1.8	**0.0310**	3.0	5.3	**0.0955**	2.5	16.4	3.08	**2.200**	8.2	377	**0.765**	*14.58*	**19.06**	1.80		
B-2 a1	94.9	**0.0237**	3.8	**0.0170**	5.1	4.3	**0.0695**	2.5	17.5	4.10	**1.303**	8.2	328	**0.829**	*4.44*	**5.36**	0.58		
B-2 a2	106.5	**0.0439**	2.8	**0.0157**	5.4	2.9	**0.0463**	2.7	8.6	2.94	**1.637**	8.2	302	**0.848**	*9.04*	**10.66**	1.07		
B-2 a3	104.1	**0.0872**	2.0	**0.0277**	3.3	7.7	**0.2261**	2.4	63.1	8.16	**1.498**	8.2	418	**0.841**	*7.71*	**9.16**	0.68		
B-2 a4	81.7	**0.0249**	3.5	**0.0103**	8.1	4.7	**0.0323**	2.8	14.7	3.14	**0.812**	8.3	371	**0.815**	*8.39*	**10.30**	1.24	**8.87**	0.89
B-3 a1	59.7	**0.1078**	2.0	**0.0457**	3.5	6.8	**0.2087**	2.5	30.9	4.57	**2.675**	2.2	396	**0.729**	*7.61*	**10.44**	1.01		
B-3 a2	90.0	**0.0332**	3.2	**0.0167**	8.9	2.9	**0.0538**	2.7	9.4	3.22	**1.362**	2.2	239	**0.834**	*6.77*	**8.11**	0.89		
B-3 a3	71.6	**0.0421**	3.1	**0.0191**	7.9	3.6	**0.0541**	2.7	10.2	2.83	**1.188**	2.2	224	**0.795**	*8.36*	**10.52**	1.19		
B-3 a4	78.0	**0.0311**	3.5	**0.0129**	11.4	2.7	**0.0386**	2.9	8.1	2.98	**0.952**	2.2	201	**0.792**	*8.61*	**10.87**	1.46	**9.99**	1.14
B-5 a1	72.7	**0.1142**	1.9	**0.0434**	2.3	6.5	**0.1261**	2.5	19.0	2.91	**2.553**	2.8	384	**0.783**	*10.02*	**12.80**	1.03		
B-5 a2	67.5	**0.0474**	2.7	**0.0131**	5.5	6.3	**0.0627**	2.6	30.2	4.78	**0.815**	3.8	392	**0.763**	*11.30*	**14.82**	1.50		
B-5 a3	90.5	**0.0109**	5.3	**0.0037**	24.7	2.2	**0.0130**	3.5	7.5	3.50	**0.439**	4.8	256	**0.821**	*8.68*	**10.57**	2.23		
B-5 a4	67.9	**0.0714**	2.2	**0.0175**	4.5	4.9	**0.0558**	2.6	15.7	3.19	**1.372**	3.1	387	**0.780**	*14.06*	**18.02**	1.62	**14.05**	1.58
B-6 a1	46.7	**0.0241**	3.5	**0.0088**	17.3	2.3	**0.0263**	3.0	6.8	2.98	**0.510**	2.2	131	**0.658**	*10.36*	**15.75**	3.12		
B-6 a2	46.8	**0.0357**	3.4	**0.0115**	13.1	2.8	**0.0358**	2.9	8.9	3.11	**0.629**	2.2	155	**0.664**	*11.73*	**17.67**	2.98		
B-6 a3	47.0	**0.0091**	5.9	**0.0042**	36.4	1.2	**0.0127**	3.0	3.7	3.02	**0.321**	2.2	93	**0.681**	*7.63*	**11.20**	3.76		
B-6 a4	52.4	**0.0274**	3.6	**0.0082**	21.1	2.2	**0.0236**	3.1	6.3	2.88	**0.537**	2.2	143	**0.709**	*12.45*	**17.57**	3.80	**15.55**	3.42
B-7 a1	55.9	**0.0422**	2.7	**0.0141**	9.9	2.9	**0.0445**	2.8	9.3	3.16	**0.979**	2.2	204	**0.712**	*10.68*	**15.00**	1.99		
B-7 a2	51.6	**0.0181**	4.3	**0.0051**	30.9	1.5	**0.0164**	3.1	4.8	3.23	**0.406**	2.2	118	**0.710**	*12.13*	**17.09**	4.70		
B-7 a3	61.3	**0.0384**	3.1	**0.0132**	11.0	2.7	**0.0427**	2.8	8.6	3.24	**1.047**	2.2	210	**0.738**	*9.95*	**13.47**	1.81	**15.19**	2.83
B-7 a4	38.3	**0.0197**	4.1	**0.0053**	27.9	1.4	**0.0154**	3.2	4.2	2.94	**0.469**	2.2	127	**0.575**	*12.77*	**22.20**	5.96		
B-8 a1	74.0	**0.0519**	2.7	**0.0257**	3.2	7.9	**0.0708**	2.5	21.7	2.75	**1.465**	3.4	449	**0.784**	*7.88*	**10.05**	0.93		
B-8 a2	57.2	**0.0326**	3.3	**0.0130**	5.7	7.4	**0.0381**	2.7	21.9	2.94	**0.822**	4.2	471	**0.717**	*9.38*	**13.09**	1.59		
B-8 a3	73.7	**0.0173**	4.3	**0.0113**	7.2	4.7	**0.0337**	2.7	14.0	2.98	**0.924**	3.9	383	**0.778**	*5.33*	**6.86**	0.86		
B-8 a4	59.1	**0.0583**	2.5	**0.0275**	2.9	5.8	**0.0862**	2.5	18.1	3.14	**1.819**	3.1	382	**0.732**	*7.67*	**10.48**	1.05	**10.12**	1.28
B-9 a1	72.6	**0.0091**	5.9	**0.0108**	7.4	8.6	**0.0311**	2.8	24.9	2.89	**0.575**	5.4	461	**0.782**	*3.29*	**4.20**	0.65		
B-9 a2	74.8	**0.0226**	3.9	**0.0175**	4.4	5.8	**0.0516**	2.6	17.0	2.94	**1.165**	3.5	384	**0.789**	*4.76*	**6.04**	0.66		
B-9 a3	63.5	**0.0497**	2.8	**0.0226**	3.3	4.8	**0.0687**	2.5	14.7	3.03	**1.495**	3.7	319	**0.747**	*8.03*	**10.75**	1.09		
B-9 a4	45.7	**0.0302**	3.2	**0.0134**	5.3	5.8	**0.0340**	2.7	14.6	2.53	**0.869**	3.7	373	**0.653**	*8.73*	**13.38**	1.79	**8.59**	2.11
B-10 a1	61.9	**0.0407**	2.9	**0.0172**	4.5	4.9	**0.0529**	2.6	15.2	3.08	**1.355**	3.5	391	**0.733**	*8.23*	**11.24**	1.22		
B-10 a2	92.2	**0.0240**	3.9	**0.0100**	7.7	4.6	**0.0320**	2.8	14.8	3.20	**0.756**	3.9	350	**0.828**	*8.35*	**10.08**	1.16		
B-10 a3	89.8	**0.1217**	1.8	**0.0404**	2.4	4.1	**0.2043**	2.4	20.7	5.06	**3.298**	2.4	334	**0.818**	*8.68*	**10.61**	0.75		
B-10 a4	57.2	**0.0447**	2.7	**0.0161**	4.5	5.6	**0.0603**	2.6	20.8	3.75	**1.261**	3.0	435	**0.715**	*9.08*	**12.71**	1.39	**11.16**	0.57
B-11 a1	76.2	**0.0356**	2.8	**0.0130**	5.5	4.2	**0.0361**	2.7	11.7	2.78	**0.922**	3.8	298	**0.790**	*10.10*	**12.79**	1.28		
B-11 a2	83.6	**0.0385**	3.0	**0.0159**	4.8	7.8	**0.0377**	2.7	18.5	2.37	**0.744**	3.7	364	**0.807**	*10.28*	**12.73**	1.25		
B-11 a3	75.3	**0.0184**	4.1	**0.0095**	7.4	8.4	**0.0234**	2.9	20.8	2.46	**0.417**	4.3	370	**0.786**	*8.22*	**10.46**	1.35		
B-11 a4	106.5	**0.0463**	2.7	**0.0193**	4.0	7.1	**0.0505**	2.6	18.5	2.61	**0.987**	3.6	361	**0.852**	*9.72*	**11.41**	0.93	**11.85**	0.56

		He		U			Th				Sm			Ejection	*Uncorr.*	Ft-Corr.		Sample unweighted aver. ± 1 s.e.	
Sample	Sphere radius [µm]	vol. [ncc]	1s [%]	mass [ng]	1s [%]	conc. [ppm]	mass [ng]	1s [%]	conc. [ppm]	Th/U ratio	mass [ng]	1s [%]	conc. [ppm]	correct. (Ft)	*He-age [Ma]*	He-age [Ma]	2s [Ma]	[Ma]	[Ma]
B-12 a1	51.2	**0.0386**	2.9	**0.0099**	17.4	2.3	**0.0401**	2.8	9.2	4.03	**0.807**	2.2	185	**0.687**	*12.25*	**17.84**	3.04		
B-12 a2	67.6	**0.0117**	5.0	**0.0065**	25.9	1.6	**0.0189**	3.3	4.6	2.93	**0.576**	2.2	141	**0.798**	*6.17*	**7.73**	1.83		
B-12 a3	45.8	**0.0289**	3.4	**0.0096**	15.9	2.5	**0.0338**	2.9	8.8	3.53	**0.644**	2.2	168	**0.646**	*10.45*	**16.16**	2.93		
B-12 a4	41.0	**0.0111**	5.3	**0.0045**	34.5	1.3	**0.0157**	3.1	4.6	3.49	**0.342**	2.2	100	**0.605**	*8.33*	**13.78**	4.34	**13.88**	3.03
B-13 a1	67.7	**0.0275**	3.6	**0.0132**	6.4	7.1	**0.0332**	2.7	17.9	2.52	**0.674**	4.8	364	**0.755**	*8.58*	**11.35**	1.39		
B-13 a2	61.5	**0.0693**	2.4	**0.0247**	3.2	5.8	**0.0790**	2.5	18.7	3.19	**1.561**	4.0	369	**0.728**	*10.18*	**14.00**	1.42		
B-13 a3	49.1	**0.0150**	4.8	**0.0076**	11.5	3.5	**0.0173**	3.2	8.0	2.29	**0.625**	4.2	289	**0.657**	*7.41*	**11.28**	1.97	**12.21**	0.89
B-13 a4	*38.4*	**0.0051**	1.8	**0.0101**	8.2	5.8	**0.0309**	2.8	17.9	3.06	**0.598**	5.0	346	**0.564**	*1.90*	**3.37**	0.53		
B-14 a1	*84.9*	**0.0702**	2.3	**0.0209**	4.1	7.9	**0.0730**	2.5	27.6	3.49	**1.214**	8.3	460	**0.810**	*12.06*	**14.89**	1.35		
B-14 a2	103.4	**0.0525**	2.8	**0.0182**	4.7	6.2	**0.0634**	2.6	21.7	3.49	**1.196**	8.3	410	**0.853**	*10.10*	**11.84**	1.07		
B-14 a3	70.8	**0.0659**	2.4	**0.0133**	6.0	3.8	**0.0759**	2.5	21.6	5.72	**1.144**	8.3	326	**0.768**	*13.39*	**17.42**	1.78		
B-14 a4	80.1	**0.0515**	2.7	**0.0120**	6.8	2.9	**0.0377**	2.7	9.0	3.14	**1.270**	8.3	302	**0.800**	*13.57*	**16.96**	1.87	**15.28**	1.52
B-15 a1	62.3	**0.0298**	3.4	**0.0115**	16.6	2.7	**0.0371**	2.8	8.9	3.24	**0.720**	2.2	172	**0.760**	*9.41*	**12.37**	2.13		
B-15 a2	44.2	**66.8515**	5.6	**0.0195**	7.9	4.7	**0.1915**	2.5	46.4	9.81	**0.821**	2.2	199	**0.629**	*5967.96*	**9489.89**	1579.42		
B-15 a3	42.6	**0.4065**	1.5	**0.2993**	1.9	76.1	**0.0104**	3.0	2.7	0.03	**0.498**	2.2	127	**0.647**	*11.01*	**17.02**	1.97		
B-15 a4	41.3	**0.0193**	4.1	**0.0080**	18.8	2.0	**0.0352**	2.9	8.9	4.39	**0.532**	2.2	135	**0.610**	*7.71*	**12.64**	2.55	**14.01**	2.22
B-16 a1	46.9	**0.0324**	3.2	**0.0100**	16.9	2.6	**0.0375**	2.8	9.8	3.77	**0.591**	2.2	154	**0.657**	*11.28*	**17.19**	3.16		
B-16 a2	41.1	**0.0197**	4.0	**0.0053**	44.6	1.5	**0.0206**	3.1	6.0	3.86	**0.431**	2.2	125	**0.603**	*11.88*	**19.69**	7.14		
B-16 a3	59.0	**0.0602**	2.6	**0.0179**	8.0	3.5	**0.0673**	2.6	13.1	3.75	**1.260**	2.2	246	**0.728**	*11.24*	**15.44**	1.80		
B-16 a4	61.1	**0.0321**	3.2	**0.0127**	12.1	3.2	**0.0491**	2.8	12.5	3.87	**0.710**	2.2	181	**0.770**	*8.81*	**11.45**	1.58	**15.94**	3.42
B-17 a1	47.7	**0.0268**	3.7	**0.0097**	15.7	2.6	**0.0401**	2.8	10.9	4.12	**0.680**	2.2	184	**0.660**	*8.93*	**13.54**	2.36		
B-17 a2	50.9	**0.0395**	3.0	**0.0081**	18.3	2.1	**0.0314**	3.0	8.1	3.85	**0.618**	2.2	159	**0.682**	*15.78*	**23.14**	4.17		
B-17 a3	36.6	**0.0285**	3.6	**0.0056**	25.6	1.7	**0.0206**	3.0	6.2	3.67	**0.403**	2.2	121	**0.562**	*17.07*	**30.35**	7.62		
B-17 a4	49.5	**0.0142**	5.3	**0.0035**	60.5	1.1	**0.0104**	3.0	3.3	3.00	**0.252**	2.2	81	**0.695**	*14.69*	**21.15**	11.07		
B-17 a5	33.3	**0.0170**	4.7	**0.0054**	13.2	6.4	**0.0182**	2.8	21.4	3.35	**0.352**	8.8	414	**0.498**	*11.08*	**22.23**	4.74		
B-17 a6	33.2	**0.0146**	4.9	**0.0028**	35.0	3.3	**0.0126**	3.2	14.5	4.44	**0.296**	8.8	340	**0.501**	*14.65*	**29.24**	8.71		
B-17 a7	56.5	**0.0622**	2.7	**0.0165**	4.8	3.9	**0.0461**	2.6	11.0	2.79	**1.219**	8.8	290	**0.710**	*13.74*	**19.36**	2.33		
B-17 a8	45.3	**0.0968**	2.2	**0.0142**	5.2	5.9	**0.0462**	2.5	19.2	3.26	**0.897**	8.8	373	**0.666**	*24.61*	**36.98**	4.66		
B-17 a9	43.1	**0.0353**	3.4	**0.0090**	6.0	3.7	**0.0307**	2.5	12.6	3.41	**0.837**	8.8	343	**0.640**	*12.59*	**19.65**	2.87		
B-17 a10	48.2	**0.0286**	4.2	**0.0079**	10.1	4.3	**0.0249**	2.6	13.5	3.17	**0.678**	8.8	367	**0.691**	*12.23*	**17.70**	2.78	**23.33**	5.13
Standard:																			
DuF a258	2.7	**2.2640**	1.9	**0.1186**	1.9	14.0	**2.0799**	2.4	244.8	17.54	**1.388**	8.8	163	**1.000**	*30.04*	**30.04**	1.62		
DuF a259	2.7	**2.4176**	1.9	**0.1230**	1.9	10.5	**2.1504**	2.4	184.3	17.48	**1.634**	8.8	140	**1.000**	*30.93*	**30.93**	1.67		
DuF a260	2.7	**2.5373**	1.9	**0.1177**	1.9	8.9	**2.3358**	2.4	176.9	19.84	**2.001**	8.8	152	**1.000**	*30.49*	**30.49**	1.66	**30.48**	1.65

Table DR7 *XRD results.*

Device	Philips X'Pert MPD
Rietveld software	AutoQuan 2.8.0.1
Tube	Cu Kα
Voltage [kV]	40
Current [mA]	30
Soller slit [rad]	0.04
Divergence slit [°]	0.5
Mask [mm]	20
Anti Scatter slit [°]	0.5
Reciving slit [mm]	0.2
Scan mode	step scan
Step (°2Theta)	0.02
Time/step [s]	10
Internal Standard	20 wt% ZnO

SiO2 (Quarz) [%]	K-Fsp [%]	Plagioclase [%]
20	46	34
6	21	73
7	27	66
22	23	54
20	17	63
19	19	62

Batch 1 Probe	Qualitätsparameter (1-rho) [%]	Mineral Phase [wt%] amorph content	±3σ	Mineral Phase [wt%] Cordierite	±3σ	Mineral Phase [wt%] Cristobalite	±3σ
SL-B-4	0.76	5.20	4.20			6.26	1.23
SL-B-5	0.63	8.37	2.91	2.86	0.42	2.32	0.81
SL-B-8	0.66	4.20	3.30			2.74	0.63
SL-B-9	0.76	2.90	4.80			11.14	2.85
SL-B-14	0.68	5.20	3.30	0.75	0.33	9.74	2.04
SL-B-17	0.75	5.40	3.30	0.20	0.28	9.20	0.99

Batch 1 Probe	Mineral Phase [wt%] Tridymite	±3σ	Mineral Phase [wt%] Diopside	±3σ	Mineral Phase [wt%] Garronite	±3σ	Mineral Phase [wt%] Goethite	±3σ
SL-B-4	9.85	0.84			1.55	1.11	1.75	0.81
SL-B-5	9.80	1.32					5.79	0.96
SL-B-8	9.56	1.44					3.19	0.84
SL-B-9	10.52	0.72			0.88	1.08	0.72	0.96
SL-B-14	4.19	1.26					4.62	1.17
SL-B-17	3.29	1.92	1.91	0.72			6.24	1.08

Batch 1 Probe	Mineral Phase [wt%] Hematite	±3σ	Mineral Phase [wt%] Kaolinite	±3σ	Mineral Phase [wt%] Microcline	±3σ	Mineral Phase [wt%] Albit	±3σ
SL-B-4	2.28	0.45	6.75	1.11	14.16	3.81	2.68	2.31
SL-B-5	1.17	0.22			7.93	2.01	2.04	0.69
SL-B-8	1.51	0.25	1.68	0.75	11.43	2.76	4.89	1.41
SL-B-9	2.27	0.39			11.56	4.05	3.40	2.19
SL-B-14	1.65	0.21			8.02	1.89	9.17	1.77
SL-B-17	1.09	0.17			9.13	1.95	7.37	1.47

Batch 1 Probe	Mineral Phase [wt%] Andesine	±3σ	Mineral Phase [wt%] Quartz	±3σ	Mineral Phase [wt%] Sanidine	±3σ	Mineral Phase [wt%] Smectite	±3σ
SL-B-4	7.70	1.74	6.02	0.45	23.37	2.73	12.40	3.30
SL-B-5	26.25	1.41	2.92	0.19	24.11	1.59	6.43	1.20
SL-B-8	23.04	1.47	3.17	0.27	24.38	1.56	10.14	1.68
SL-B-9	23.49	1.59	2.52	0.36	22.30	2.85	8.75	2.85
SL-B-14	21.38	1.56	4.28	0.21	25.81	1.80	5.18	1.05
SL-B-17	22.81	1.68	1.10	0.14	27.16	1.71	5.16	1.41

Figure DR6 *Laser ablation profiling perpendicular to the c-axis.*

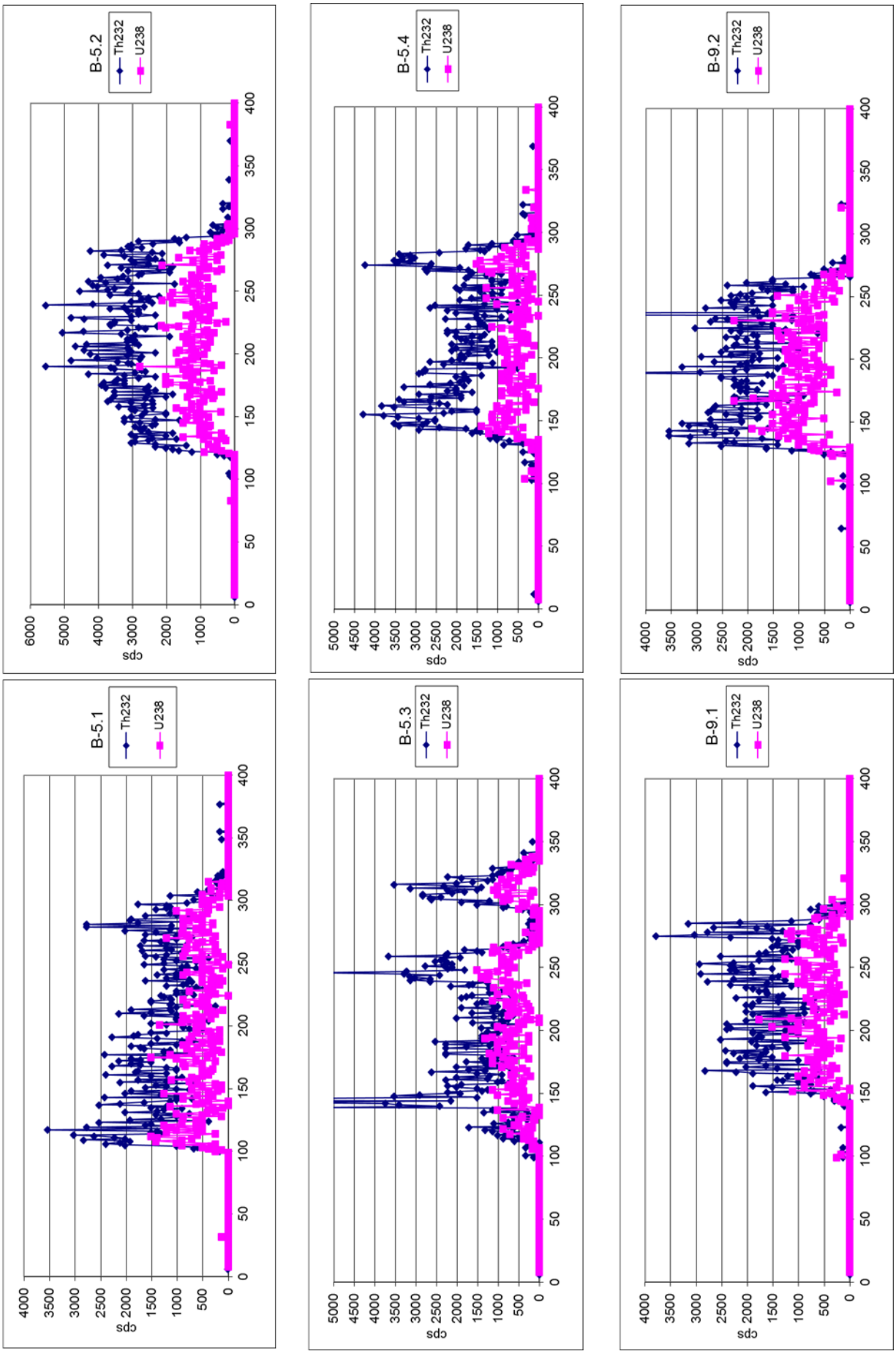

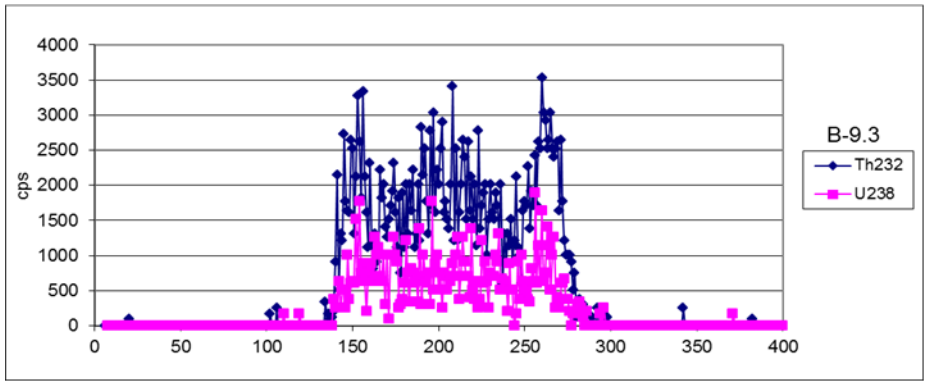
B-9.3
cps
Th232
U238
0
500
1000
1500
2000
2500
3000
3500
4000
0
50
100
150
200
250
300
350
400

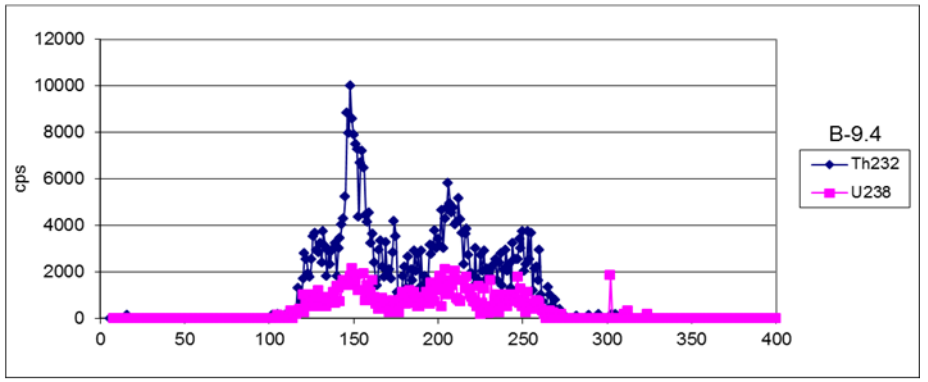
B-9.4
cps
Th232
U238
0
2000
4000
6000
8000
10000
12000
0
50
100
150
200
250
300
350
400

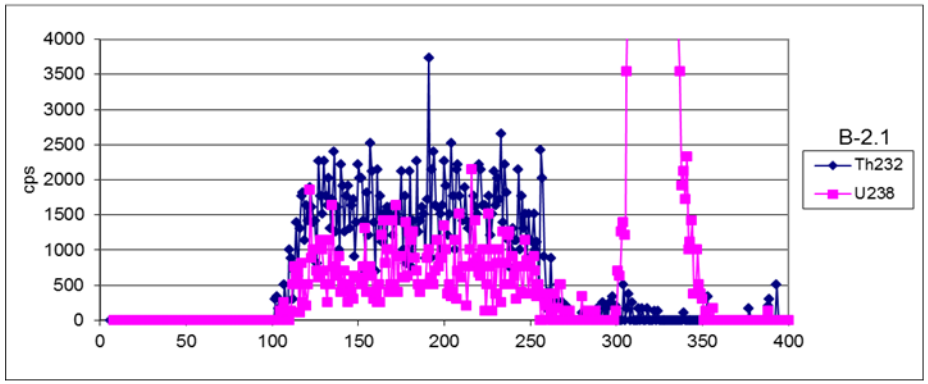
B-2.1
cps
Th232
U238
0
500
1000
1500
2000
2500
3000
3500
4000
0
50
100
150
200
250
300
350
400

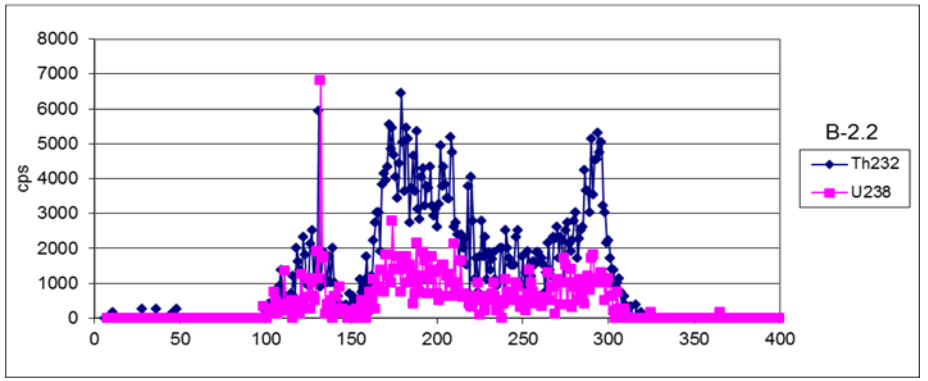
B-2.2
cps
Th232
U238
0
1000
2000
3000
4000
5000
6000
7000
8000
0
50
100
150
200
250
300
350
400

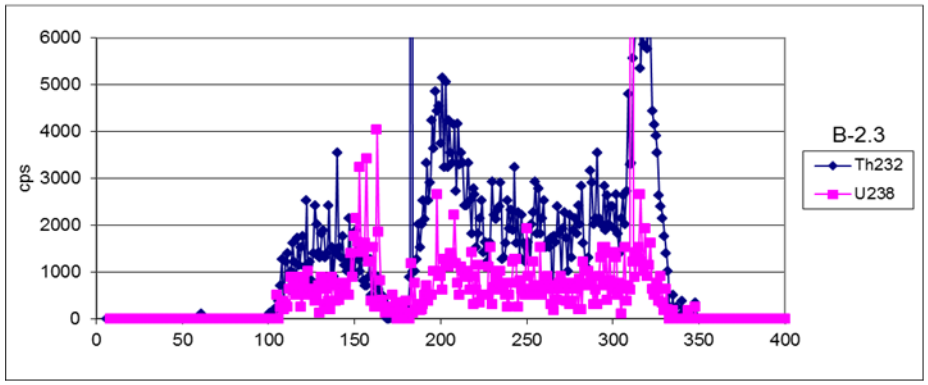
B-2.3
cps
Th232
U238
0
1000
2000
3000
4000
5000
6000
0
50
100
150
200
250
300
350
400

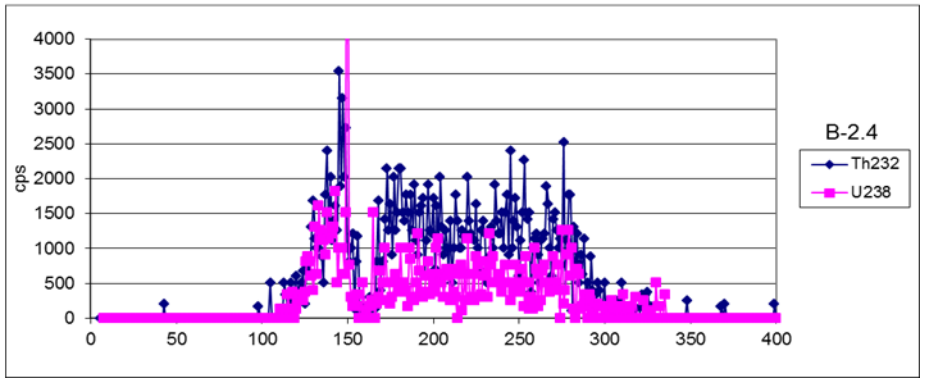
B-2.4
cps
Th232
U238
0
500
1000
1500
2000
2500
3000
3500
4000
0
50
100
150
200
250
300
350
400

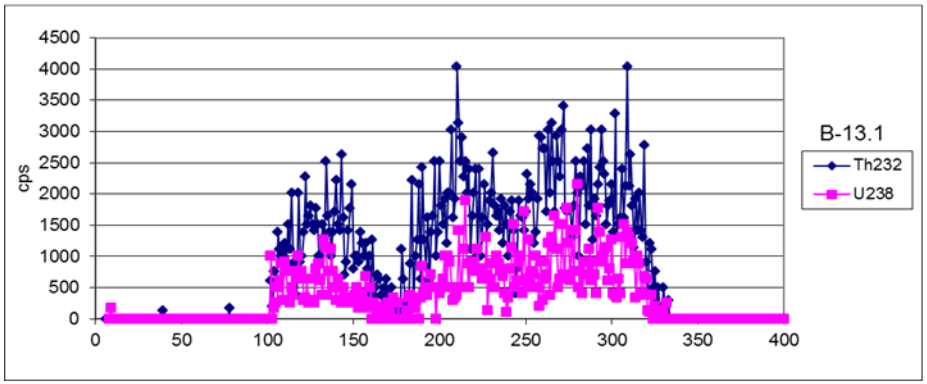
B-13.1
Th232
U238
cps
4500
4000
3500
3000
2500
2000
1500
1000
500
0
0
50
100
150
200
250
300
350
400

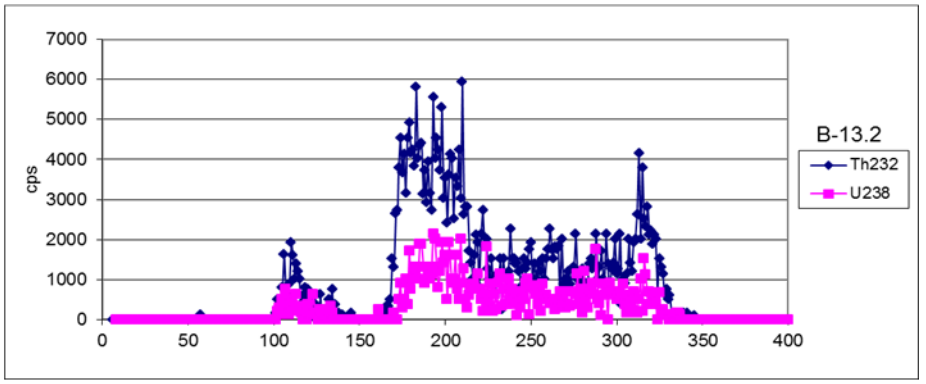
B-13.2
Th232
U238
cps
7000
6000
5000
4000
3000
2000
1000
0
0
50
100
150
200
250
300
350
400

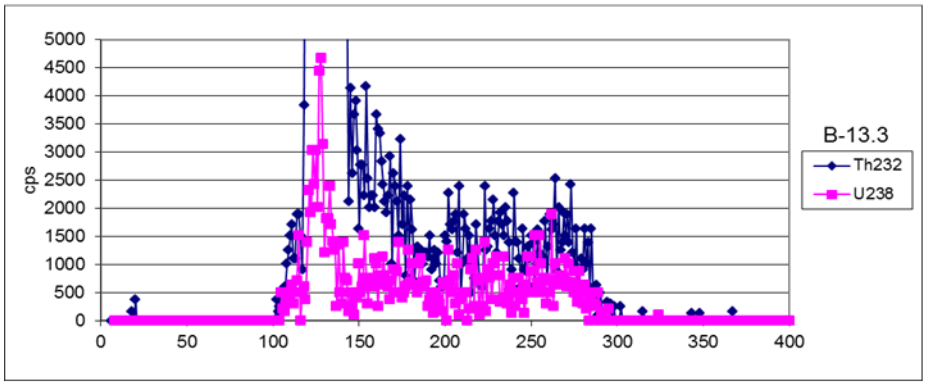
B-13.3
Th232
U238
cps
5000
4500
4000
3500
3000
2500
2000
1500
1000
500
0
0
50
100
150
200
250
300
350
400

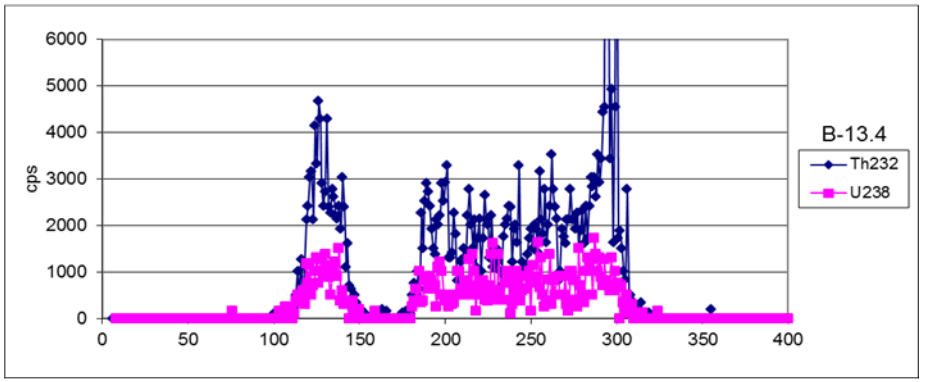
B-13.4
Th232
U238
cps
6000
5000
4000
3000
2000
1000
0
0
50
100
150
200
250
300
350
400

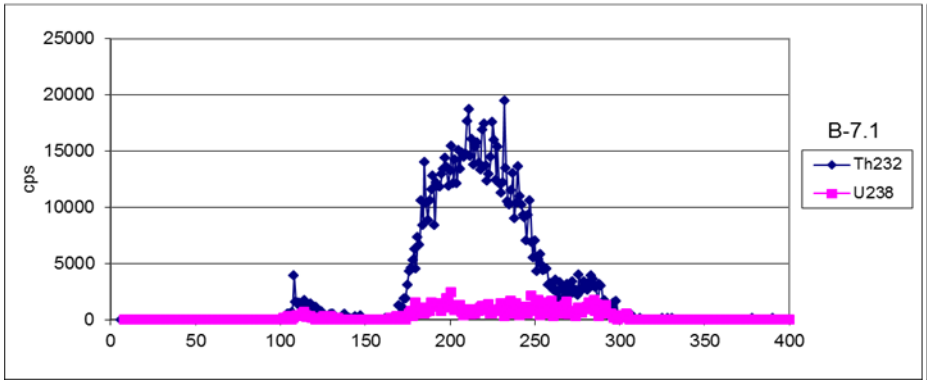
B-7.1
Th232
U238
cps
25000
20000
15000
10000
5000
0
0
50
100
150
200
250
300
350
400

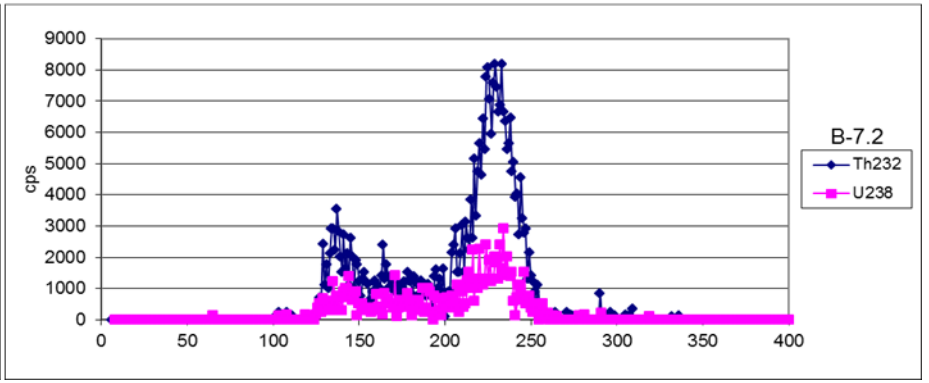
B-7.2
Th232
U238
cps
9000
8000
7000
6000
5000
4000
3000
2000
1000
0
0
50
100
150
200
250
300
350
400

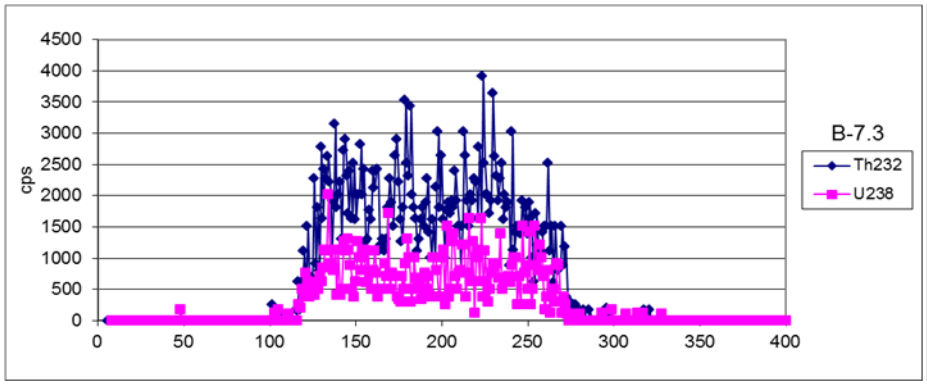
B-7.3
Th232
U238
cps
4500
4000
3500
3000
2500
2000
1500
1000
500
0
0 50 100 150 200 250 300 350 400

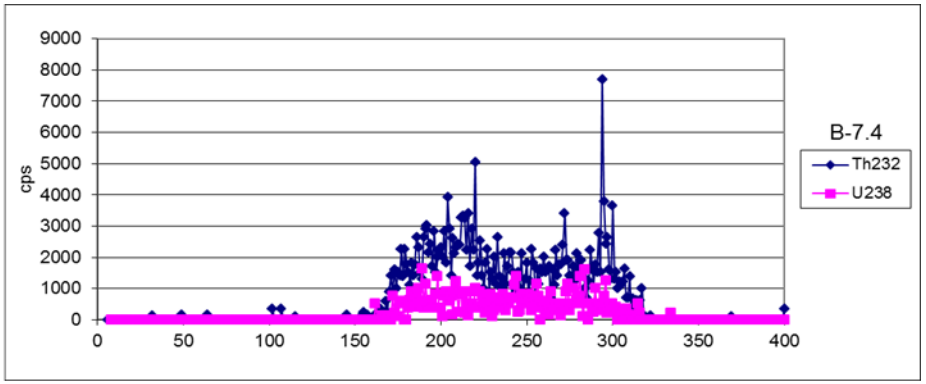
B-7.4
Th232
U238
cps
9000
8000
7000
6000
5000
4000
3000
2000
1000
0
0 50 100 150 200 250 300 350 400

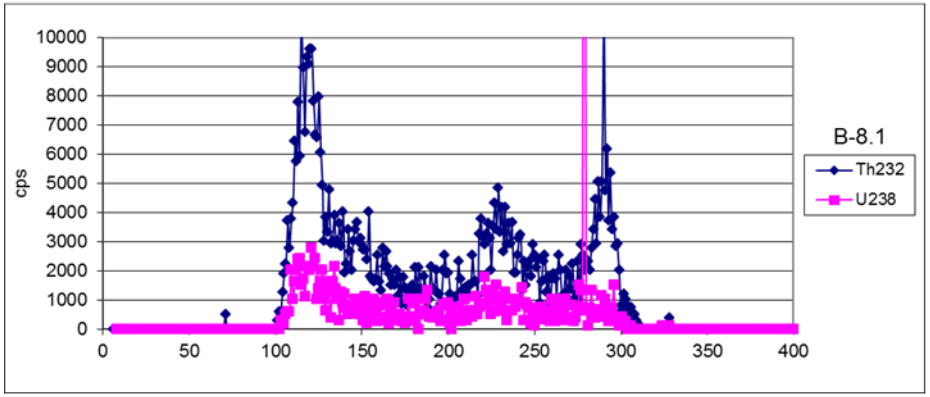
B-8.1
Th232
U238
cps
10000
9000
8000
7000
6000
5000
4000
3000
2000
1000
0
0 50 100 150 200 250 300 350 400

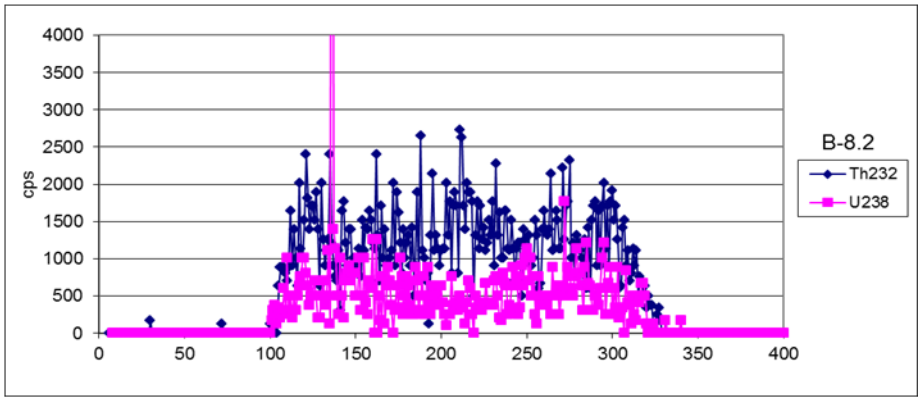
B-8.2
Th232
U238
cps
4000
3500
3000
2500
2000
1500
1000
500
0
0 50 100 150 200 250 300 350 400

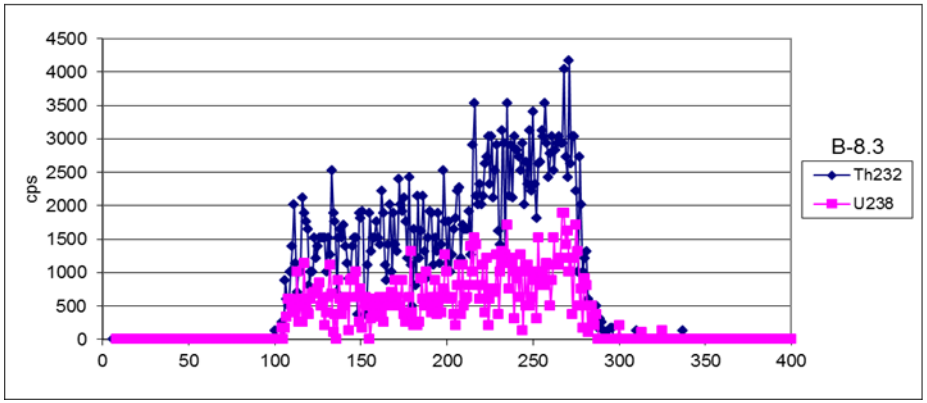
B-8.3
Th232
U238
cps
4500
4000
3500
3000
2500
2000
1500
1000
500
0
0 50 100 150 200 250 300 350 400

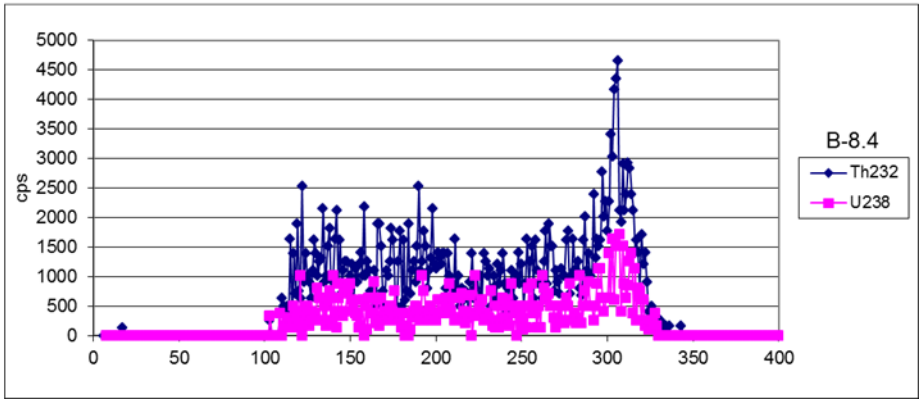
B-8.4
Th232
U238
cps
5000
4500
4000
3500
3000
2500
2000
1500
1000
500
0
0 50 100 150 200 250 300 350 400

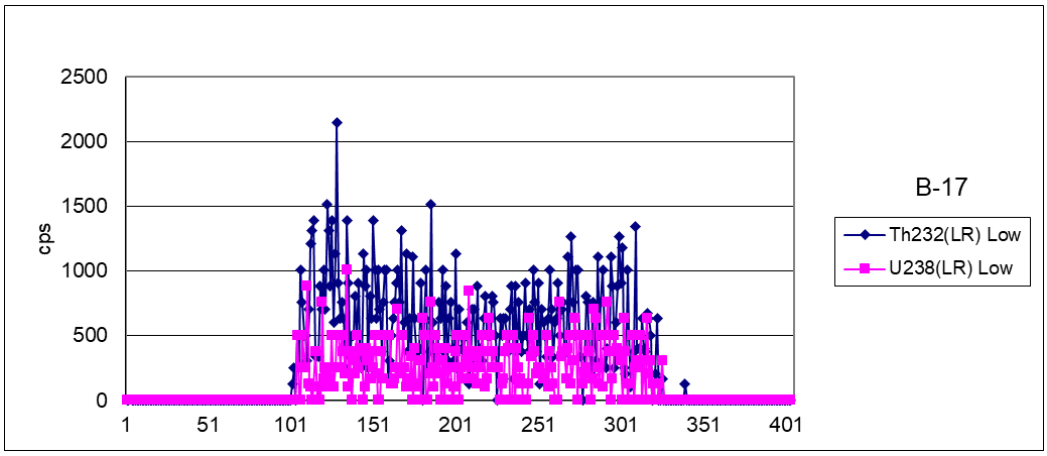

Figure DR7 *Concordia plots of U-Pb age of samples B-2, B-8 and B-9*

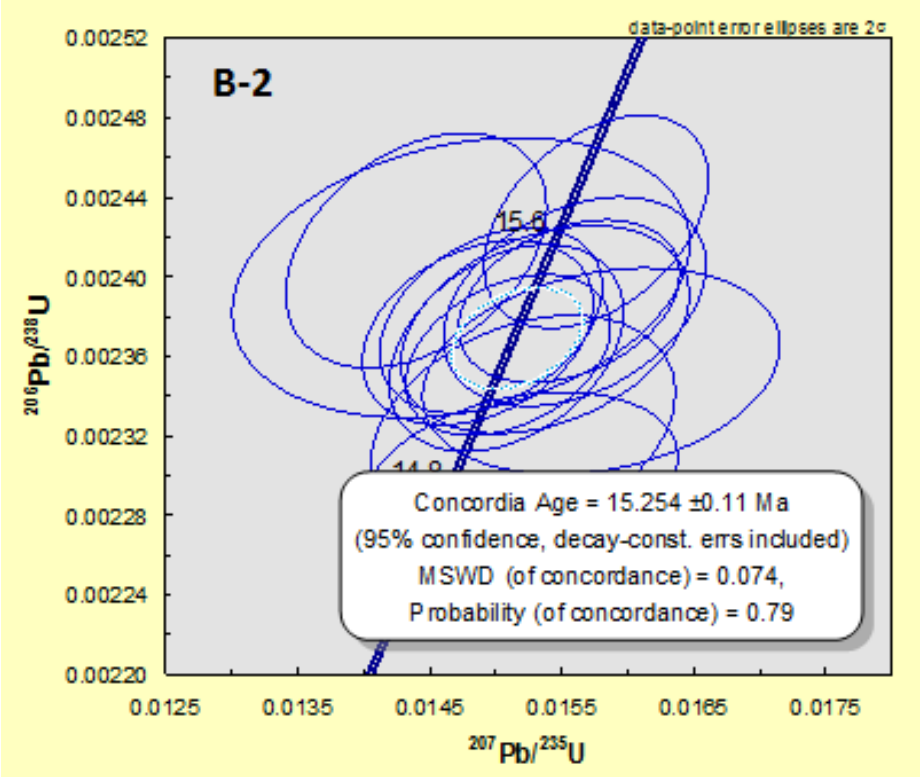

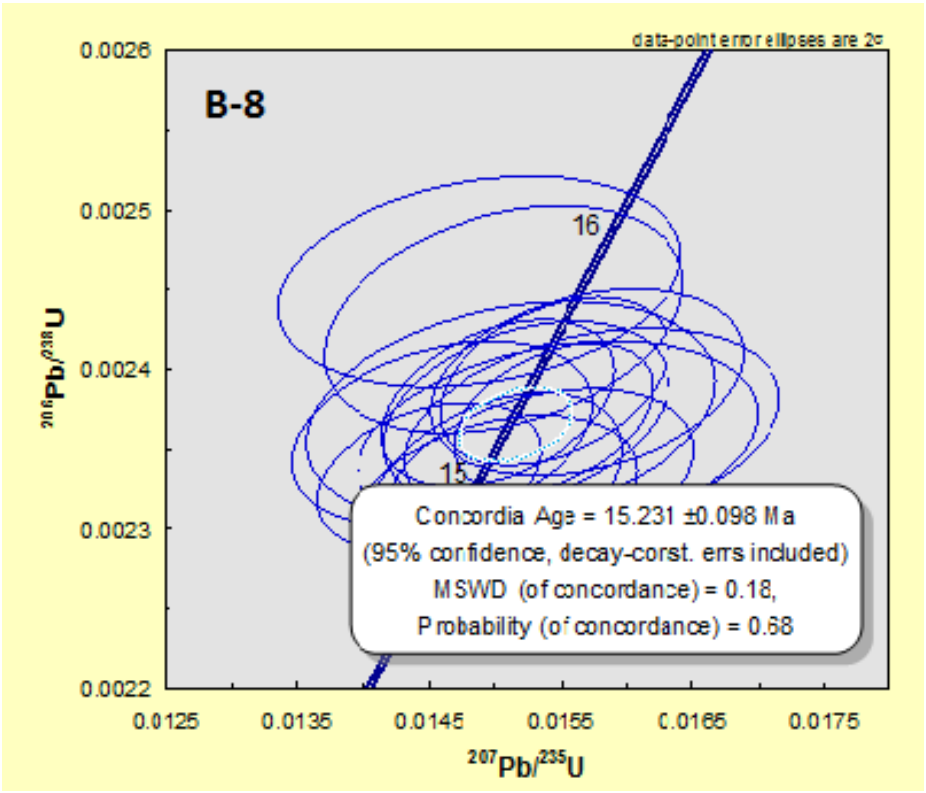
data-point error ellipses are 2σ
B-8
16
15
Concordia Age = 15.231 ±0.098 Ma
(95% confidence, decay-corst. errs included)
MSWD (of concordance) = 0.18,
Probability (of concordance) = 0.68
0.0026
0.0025
0.0024
0.0023
0.0022
0.0125
0.0135
0.0145
0.0155
0.0165
0.0175
206Pb/238U
207Pb/235U

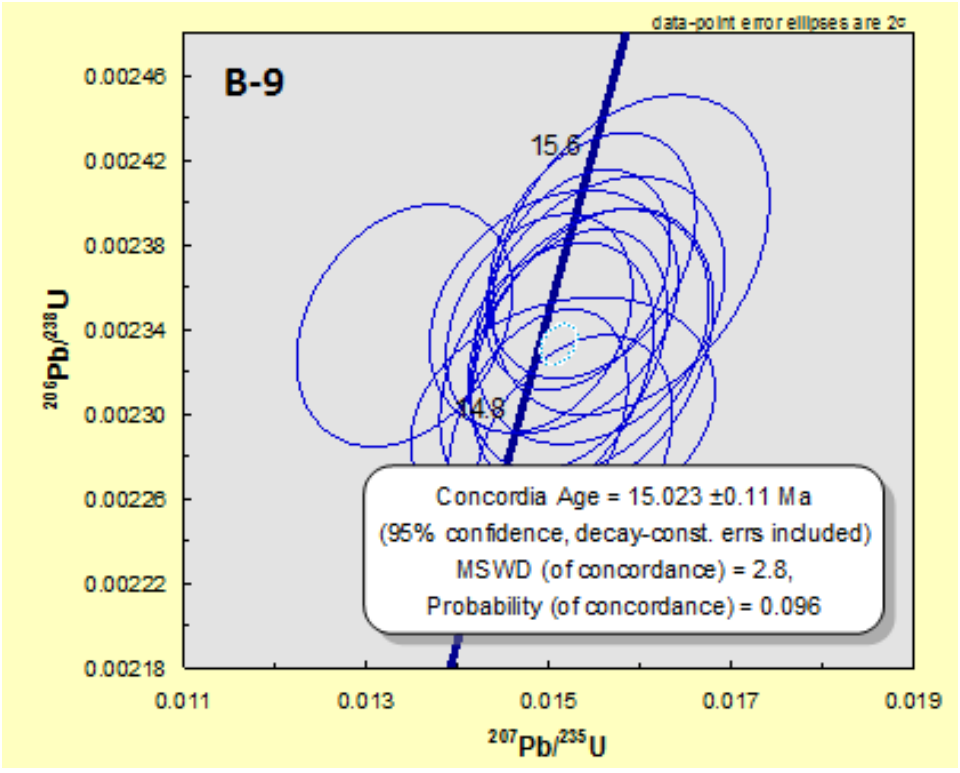
data-point error ellipses are 2σ
B-9
15.6
14.8
Concordia Age = 15.023 ±0.11 Ma
(95% confidence, decay-const. errs included)
MSWD (of concordance) = 2.8,
Probability (of concordance) = 0.096
0.00246
0.00242
0.00238
0.00234
0.00230
0.00226
0.00222
0.00218
0.011
0.013
0.015
0.017
0.019
206Pb/238U
207Pb/235U

DR2.3: Model sensitivity analysis

The sensitivity of the modeled AHe ages to specified vertical fluid flux, fault damage zone width, background thermal gradient, aerodynamic resistance, duration and exhumation rate were tested by changing one parameter at a time while keeping all other parameters at their base values. The impact of each parameter on the modeled width of the partial and full reset zone on one side of the Malpais Fault is shown in Figures DR8A, B and DR8C, D, respectively. The partial reset zone is the zone where modeled AHe ages at the surface are less than 75% of their crystallization age, and the full reset zone is the zone where AHe ages at the surface are 0.1 Ma or lower. Over long time scales, the host rock adjacent to the normal fault is heated due to conduction. This causes a rejuvenation of AHe ages in these rocks, with ages younger than the crystallization age referred to as partially reset and zero ages as fully reset.

As seen in Figure DR8, the partial and full reset zone increases with increasing hydrothermal activity. Fluid flux has a strong influence on the width of the partial reset zone perpendicular to the hydrothermally active fault for low flow rates. As fluid flux increases and reaches boiling temperatures at the surface, the differences become smaller. At high flow rates, this parameter becomes less sensitive. Same counts for background thermal gradient. Exhumation and duration of hydrothermal activity are highly sensitive parameters. In general, the relationship between the runtime and the partial reset zone is relatively linear. Notice the scale of the y-axis (Figure DR8C and D) in comparison to the y-axis of the parameters fluid flux, damage zone width, aerodynamic resistance and background thermal gradient. A relatively small increase in exhumation rates causes a large increase in the width of the partial reset zone to either side of a hydrothermally active area. The longer the hydrothermal system is active, the larger is the effect of exhumation on (U-Th)/He ages at a given thermal gradient. Thus, if there is hydrothermal activity on geological time scales, the area where AHe ages are rejuvenated becomes very large when exhumation or erosion take place at rates exceeding 1×10^{-4} m a^{-1}. A similar relationship was found for duration. If a hydrothermal system is only active for a short time, the host rock is only slightly affected from thermal rejuvenation. However, if the hydrothermal system is active for a long time scale, the area of partially reset AHe ages in the host rock becomes very large. The reason for this is two-fold. First, heat conduction heats up rocks adjacent to the fault over time. The heating is strongest in the subsurface, where temperatures are not buffered by the relatively constant air temperature. Second, exhumation brings rocks to the surface that have not been buffered by air

temperatures, the longer the duration, the deeper the origin of the rocks at the surface and the lower the effect of the buffering of air temperatures.

The least sensitive parameters are aerodynamic resistance, which governs heat flux from the land surface, and the width of the fault damage zone. Since temperatures in the Beowawe system are limited by boiling temperatures, the heat flux from the surface is relatively constant. The width of the fault damage zone changes the size of the partial reset zone, but the change is proportional to the change in width. The parameters of the full reset zone behave similar to those of the partial reset zone regarding their sensitivities. It just takes a much longer time for the AHe system to be fully reset than for them being partially reset. They also differ in their slope. At first the full reset zone grows faster as hydrothermal activity continues. Over larger time scales the slope flattens and the full reset zone becomes wider at a slower rate.

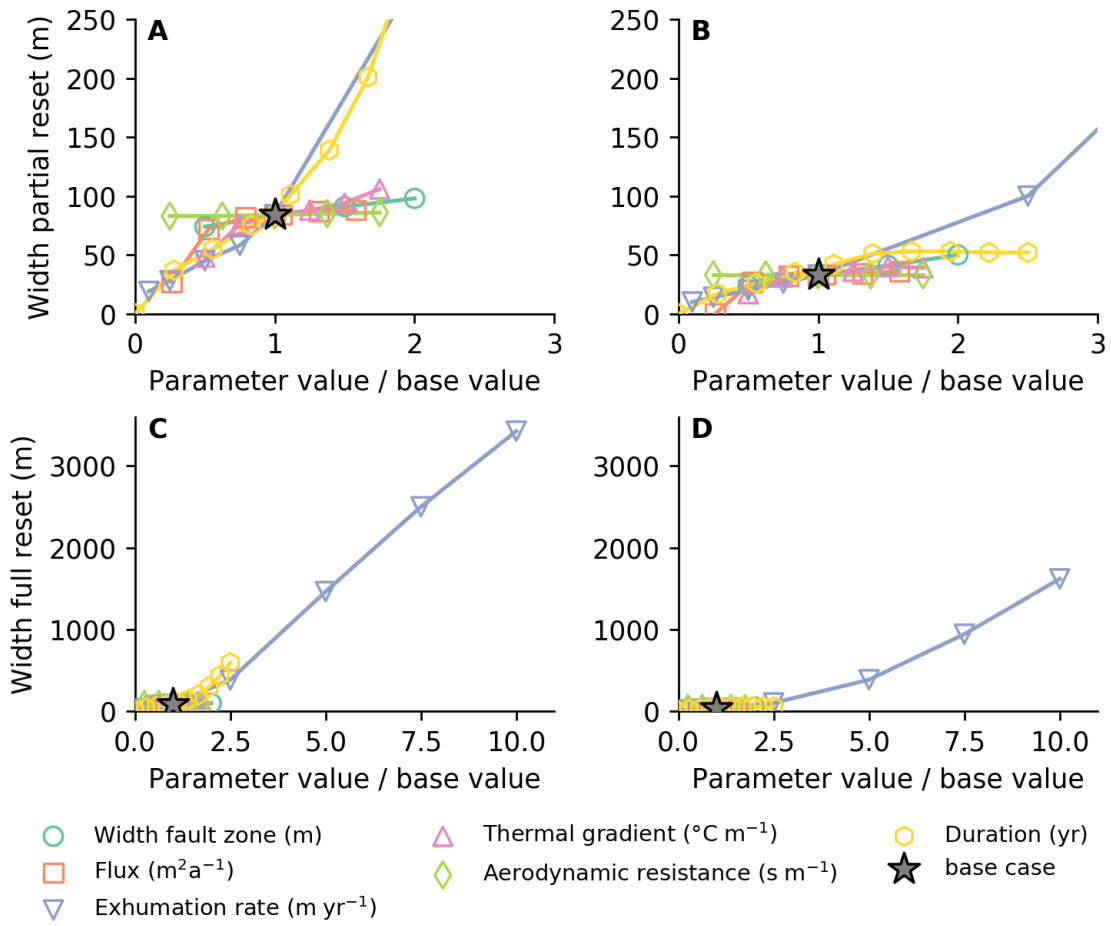

Figure DR8: *Sensitivity of the size of the zone adjacent to one side of the hydrothermally active normal fault where AHe ages are partially reset. The analysis was performed for six parameters: duration, fluid flux, fault damage zone width, background thermal gradient,*

aerodynamic resistance and exhumation rate. For each line in the graph, one parameter was changed while all other parameters were set to their base values. Base values (star) are 400 $m^2\ a^{-1}$ for the fluid flux, 10 m for the fault damage zone, 0.04 °C m^{-1} for the thermal gradient and 1×10^{-4} m a^{-1} for the exhumation rate. Lateral flow in shallow layers connected to the fault was not taken into account. The most sensitive parameter is exhumation rate. An increase in exhumation rates leads to an exponential growth of the partial reset zone. The sensitivity for fluid flux, thermal gradient and fault damage zone are in a similar order of magnitude. Fluid flux and thermal gradient are more sensitive for small values and less sensitive for larger values. Fault damage zone and aerodynamic resistance are the least sensitive parameters.

DR2.4: Model-data comparison

In addition to the results along profile B-B' that are show in the main manuscript we also modeled thermal history in profiles A-A' and C-C' as show in figure DR9 and DR10. These are models of continuous hydrothermal activity, and show comparable results to profile B-B' with the best fits for activity of 90,000 to 150,000 years in profile A-A' and 70,000 to 100,000 years in profile C-C'.

We tested the effects of different durations of episodic fluid flow and recovery times, which are shown in Figure DR11. The results show that continuous fluid flow and episodic fluid flow with a duration of 2000 years would result in zero AHe ages near the Malpais fault (panel C) and a high mean absolute error between the modeled and measured AHe ages (panel B). In contrast, models with episodic fluid flow of 1000 years and a recovery time of 6500 or 9000 years result in a much better fit of the model to the AHe data.

The significant dispersion of the single grain ages means that even the best model still has a mean absolute error of the modeled and measured single grain AHe ages of 2.0 Ma. However, the model results are relatively robust for the duration of individual fluid flow pulses. Flow duration of 500 years does not result in significant younging of AHe ages, and flow durations of 2000 years result in fully reset AHe ages. Both models do not match the partially reset AHe ages found in most of the samples close the Malpais fault, and therefore the duration of individual flow events of 1000 years is relatively robust. On the other hand, the total number of pulses that is required to match the data is much more sensitive to the actual age of the partially reset samples and is therefore less robust. Following the model experiments a difference in AHe age of 2 Ma represents a duration of approximately 80,000

years and 8 cycles of heating and thermal recovery for the best fit model (Fig. DR11C). Therefore, we estimate the uncertainty of the age of the hydrothermal activity to be approximately ±80,000 years.

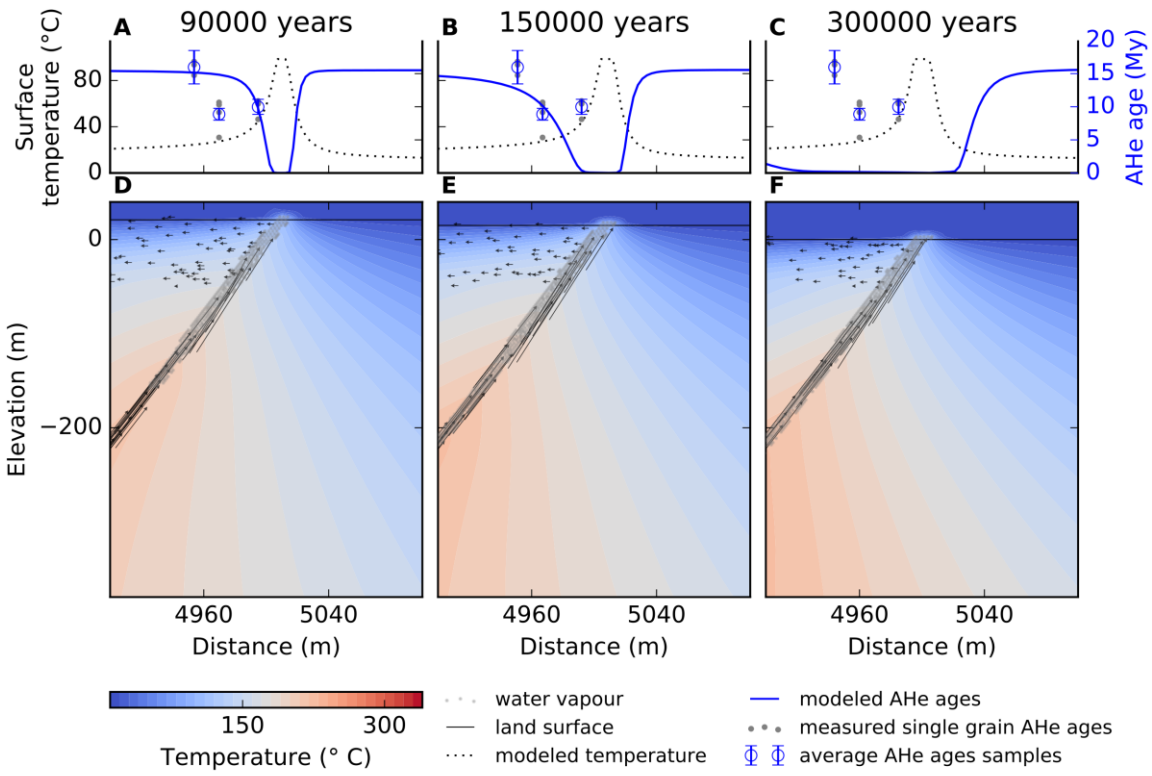

Figure DR9: *Modeled temperatures over long (ka) timescales around the Malpais fault and a comparison with measured apatite (U-Th)/He samples at the surface for profile A-A' at the western part of the sinter terrace. Panel A to C show the modeled surface temperatures, modeled AHe ages and measured AHe ages for four time slices. The lower panels (D-F) show the modeled temperature field around the Malpais fault along with flow vectors and locations where the vapor pressure curve was exceeded. The best fit of the model was obtained for a duration of hydrothermal activity of 90,000 to 150,000 years (panels A and B). See figure DR1 for the location of profile A-A'.*

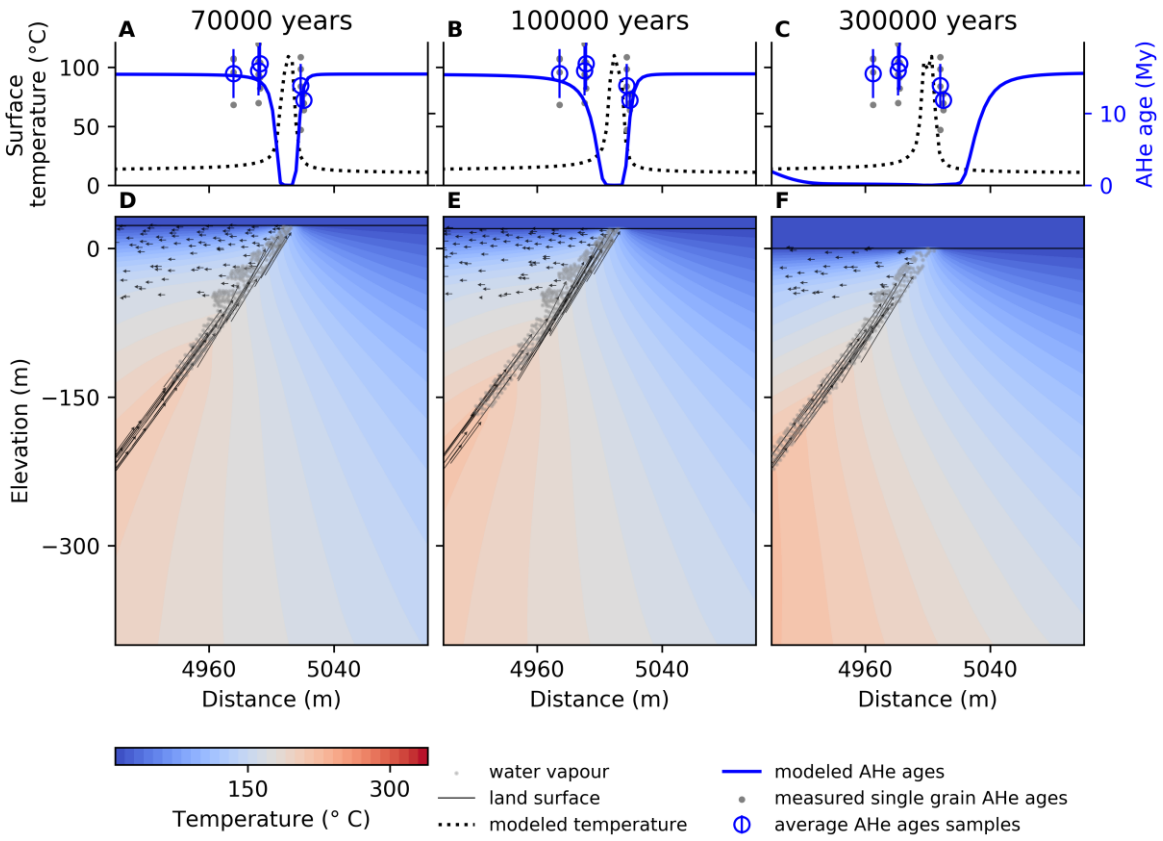

Figure DR10: *Modeled temperatures over long (ka) timescales around the Malpais fault and a comparison with measured apatite (U-Th)/He samples at the surface for profile C-C' at the central part of the sinter terrace. The best fit of the model was obtained for a duration of hydrothermal activity of around 100,000 years (panels A and B).*

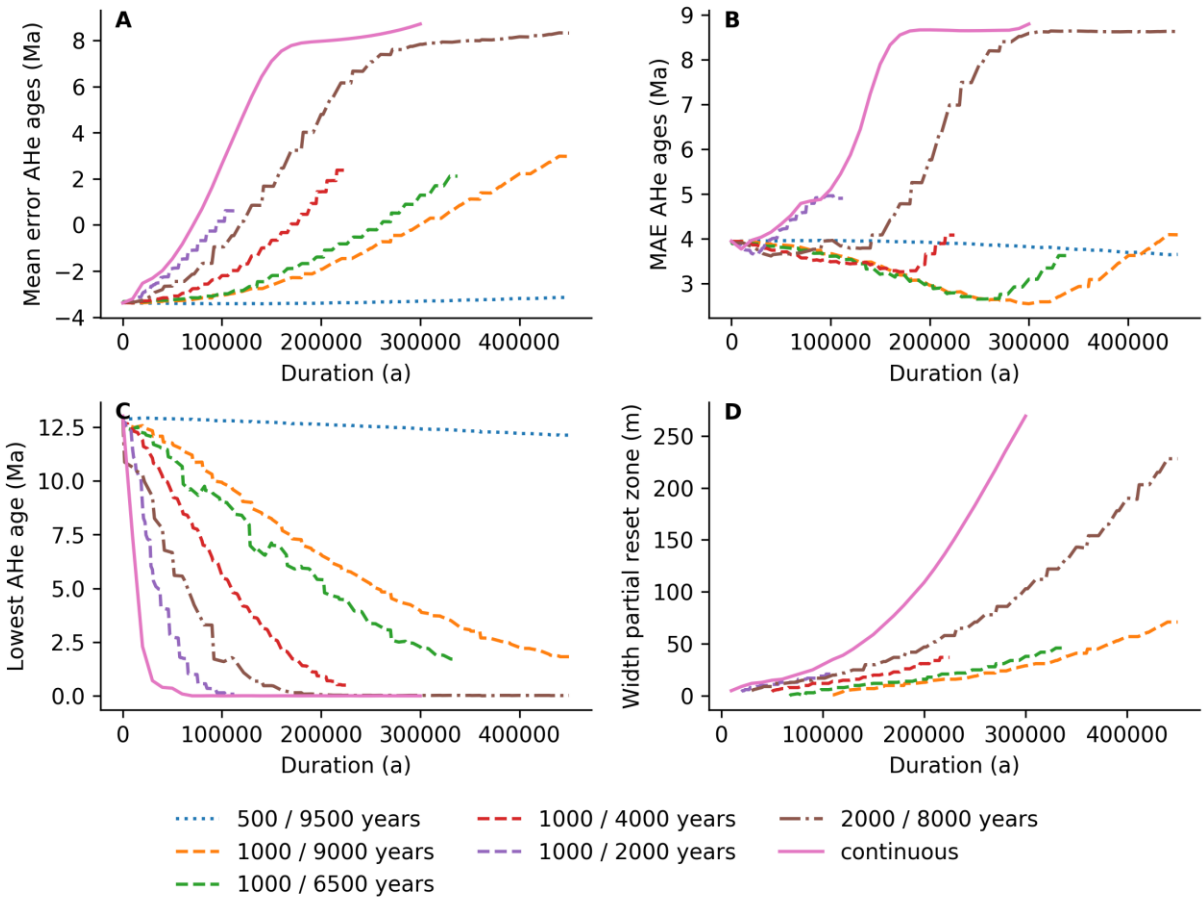

Figure DR11: *Model error (panel A, B), lowest modeled AHe age (C) and size of the zone where AHe ages (D) are partially reset for model runs various durations of fluid flow and recovery times. The results are shown for profile B-B', which had the highest density of AHe data. The results show the lowest misfit between the modeled and measured AHe ages for episodic fluid flow with 1000 years of heating and 9000 years of recovery for a total duration of 340,000 years. 1000/9000 denotes 1000 years of fluid flow followed by 9000 years of thermal recovery. Model error was calculated as the mean (A) or mean absolute difference (B) between the modeled and measured single grain AHe ages.*

REFERENCES CITED

Banerjee, A. et al., 2011, Deep permeable fault-controlled helium transport and limited mantle flux in two extensional geothermal systems in the Great Basin, United States: Geology, v. 39, p. 195–198, doi:10.1130/G31557.1.

Bateni, S.M., and Entekhabi, D., 2012, Relative efficiency of land surface energy balance components: Water Resources Research, v. 48, p. 1–8, doi:10.1029/2011WR011357.

Bense, V.F., Gleeson, T., Loveless, S.E., Bour, O., and Scibek, J., 2013, Fault zone hydrogeology: Earth-Science Reviews, v. 127, p. 171–192, doi:10.1016/j.earscirev.2013.09.008.

Braun, J., Van Der Beek, P., and Batt, G., 2006, Quantitative Thermochronology: 258 p., doi:10.1017/CBO9781107415324.004.

Caine, J., Evans, J.P., and Forster, C.B., 1996, Fault zone architecture and permeability structure: Geology, v. 24, p. 1025–1028.

Chevron Resource Company, 1979, Shallow temperature hole log.:

Childs, C., Manzocchi, T., Walsh, J.J., Bonson, C.G., Nicol, A., and Schöpfer, M.P.J., 2009, A geometric model of fault zone and fault rock thickness variations: Journal of Structural Geology, v. 31, p. 117–127, doi:10.1016/j.jsg.2008.08.009.

Dunkl, I., Mikes, T., Simon, K., and von Eynatten, H., 2008, Brief introduction to the Windows program Pepita: data visualization, and reduction, outlier rejection, calculation of trace element ratios and concentrations from LA-ICP-MS data, *in* Sylvester, P. ed., Laser ablation ICP-MS in the Earth Sciences: Current practices and outstanding issues, Vancouver, British Columbia, Mineralogical Association of Canada, p. 334–340.

Farley, K.A., 2000, Helium diffusion from apatite: General behavior as illustrated by Durango fluorapatite: Journal of Geophysical Research, v. 105, p. 2903–2914, doi:10.1029/1999JB900348.

Flowers, R.M., Ketcham, R.A., Shuster, D.L., and Farley, K.A., 2009, Apatite (U-Th)/He thermochronometry using a radiation damage accumulation and annealing model: Geochimica et Cosmochimica Acta, v. 73, p. 2347–2365, doi:10.1016/j.gca.2009.01.015.

Freeze, R.A., and Cherry, J.A., 1979, Groundwater: Upper Saddle River, NJ 07458, Prentice Hall, Inc., 604 p.

Frei, D., and Gerdes, A., 2009, Precise and accurate in situ U-Pb dating of zircon with high sample throughput by automated LA-SF-ICP-MS: Chemical Geology, v. 261, p. 261–270, doi:10.1016/j.chemgeo.2008.07.025.

Garg, S.K., Pritchett, J.W., Wannamaker, P.E., and Combs, J., 2007, Characterization of geothermal reservoirs with electrical surveys: Beowawe geothermal field: Geothermics, v. 36, p. 487–517, doi:10.1016/j.geothermics.2007.07.005.

Gosse, J.C., Harrington, C.D., and Whitney, J.W., 1995, Applications of in situ cosmogenic nuclides in the geologic site characterization of Yucca Mountain, Nevada: Cambridge University Press.

Gross, L., Bourgouin, L., and Hale, A.J., 2007a, Interface modeling in incompressible media using level sets in Escript.pdf: Physics of the Earth and Planetary Interiors, v. 163, p. 23–34, doi:doi:10.1088/1742-2132/13/2/S59.

Gross, L., Cumming, B., Steube, K., and Weatherley, D., 2007b, A Python Module for PDE-Based Numerical Modelling, *in* Kågström, B., Elmroth, E., Dongarra, J., and Waśniewski, J. eds., Applied Parallel Computing. State of the Art in Scientific Computing SE - 33, Springer Berlin Heidelberg, Lecture Notes in Computer Science, v. 4699, p. 270–279, doi:10.1007/978-3-540-75755-9_33.

Herman, F., Seward, D., Valla, P.G., Carter, A., Kohn, B., Willett, S.D., and Ehlers, T.A., 2013, Worldwide acceleration of mountain erosion under a cooling climate: Nature, v. 504, p. 423–426.

Hoang, V.T., James, E.D., and Epperson, I.J., 1987, Development Drilling, Testing and Initial Production of the Beowawe Geothermal Field: Proceedings Twelfth Workshop on Geothermal Reservoir Engineering, p. 159–162.

Howald, T. et al., 2016, Evidence for long-timescale (>103 years) changes in hydrothermal activity induced by seismic events, *in* Gleeson, T. and Ingebritsen, S.E. eds., Crustal Permeability, Chichester, Wiley-Blackwell, p. 260–274, doi:10.1002/9781119166573.ch21.

Howald, T. et al., 2015, Evidence for long timescale (>103 years) changes in hydrothermal activity induced by seismic events: Geofluids, v. 15, p. 252–268, doi:10.1111/gfl.12113.

Iovenitti, J.L., and Epperson, Jr., I.J., 1981, Beowawe Geothermal Area Evaluation Program - Final Report:, doi:10.2172/6509007.

Jackson, S.E., Pearson, N.J., Griffin, W.L., and Belousova, E.A., 2004, The application of laser ablation-inductively coupled plasma-mass spectrometry to in situ U-Pb zircon geochronology: Chemical Geology, v. 211, p. 47–69, doi:10.1016/j.chemgeo.2004.06.017.

Jungers, M.C., and Heimsath, A.M., 2016, Post-tectonic landscape evolution of a coupled basin and range: Pinaleño Mountains and Safford Basin, southeastern Arizona: Bulletin

of the Geological Society of America, v. 128, p. 469–486, doi:10.1130/B31276.1.

Ketcham, R. a., 2005, Forward and Inverse Modeling of Low-Temperature Thermochronometry Data: Reviews in Mineralogy and Geochemistry, v. 58, p. 275–314, doi:10.2138/rmg.2005.58.11.

Leatherman, M., 2010, Geochemistry and Reaction Path Modelling of the Beowawe Hydrothermal System, Nevada: A Barren End-Member Epithermal System [M.Sc. thesis]: University of Missouri-Columbia, 1-122 p.

Ludwig, K.R., 2012, User's Manual for Isoplot 3.75, a geochronological toolkit for Microsoft Excel: Berkeley Geochronology Center Special Publication, p. 1–72.

Luijendijk, E., 2019, Beo v1.0: Numerical model of heat flow and low-temperature thermochronology in hydrothermal systems: Geoscientific Model Development Discussions, p. 1–17, doi:10.5194/gmd-2018-341.

Marillo-Sialer, E., Woodhead, J., Hergt, J., Greig, A., Guillong, M., Gleadow, A., Evans, N., and Paton, C., 2014, The zircon "matrix effect": Evidence for an ablation rate control on the accuracy of U-Pb age determinations by LA-ICP-MS: Journal of Analytical Atomic Spectrometry, v. 29, p. 981–989, doi:10.1039/c4ja00008k.

Meesters, A.G.C.A., and Dunai, T.J., 2002a, Solving the production–diffusion equation for finite diffusion domains of various shapes Part I. Implications for low-temperature (U–Th)/He thermochronology: Chemical Geology, v. 186, p. 333–344, http://www.sciencedirect.com/science/article/pii/S0009254101004223.

Meesters, A.G.C.A., and Dunai, T.J., 2002b, Solving the production–diffusion equation for finite diffusion domains of various shapes Part II. Application to cases with a-ejection and nonhomogeneous distribution of the source: Chemical Geology, v. 186, p. 57–73.

Nolan, T.B., and Anderson, G.H., 1934, The geyser area near Beowawe, Eureka County: American Journal of Science, v. 27, p. 215–229.

Olmsted, F.H., and Rush, F.E., 1987, Hydrogeologic reconnaissance of the beowawe geysers geothermal area, Nevada: Geothermics, v. 16, p. 27–46, doi:10.1016/0375-6505(87)90077-0.

Poulet, T., Gross, L., Georgiev, D., and Cleverley, J., 2012, Escript-RT: Reactive transport simulation in Python using escript: Comput. Geosci., v. 45, p. 168–176, doi:10.1016/j.cageo.2011.11.005.

Riebe, C.S., Kirchner, J.W., Granger, D.E., and Finkel, R.C., 2000, Erosional equilibrium and disequilibrium in the Sierra Nevada, inferred from cosmogenic 26Al and 10Be in alluvial sediment: Geology, v. 28, p. 803–806, doi:10.1130/0091-

7613(2000)28<803:EEADIT>2.0.CO;2.

Sibbett, B.S., 1983, Structural Control and Alteration at Beowawe KGRA, Nevada: Geothermal Resources Council, Transactions, v. 7, p. 187–191, doi:10.1002/yd.430.

Sláma, J. et al., 2008, Plesovice zircon - A new natural reference material for U-Pb and Hf isotopic microanalysis: Chemical Geology, v. 249, p. 1–35, doi:10.1016/j.chemgeo.2007.11.005.

Sliwinski, J.T., Guillong, M., Liebske, C., Dunkl, I., von Quadt, A., and O., B., 2017, Improved accuracy of LA-ICP-MS U-Pb ages of Cenozoic zircons by alpha dose correction: Chemical Geology, v. 472, p. 8–21, doi:10.1016/J.CHEMGEO.2017.09.014.

Smith, C., 1983, Thermal hydrology and heat flow of Beowawe geothermal area, Nevada: Geophysics, v. 48, p. 618–626, doi:10.1190/1.1441492.

Stockli, D.F., Surpless, B.E., Dumitru, T.A., and Farley, K.A., 2002, Thermochronological constraints on the timing and magnitude of Miocene and Pliocene extension in the central Wassuk Range, western Nevada: Tectonics, v. 21, p. 10–19, doi:10.1029/2001TC001295.

Struhsacker, E.M., 1980, The Geology of the Beowawe Geothermal System, Eureka and Lander Counties, Nevada: University of Utah Research Institute, Earth Science Laboratory, p. 1–78.

Wesnousky, S.G., Barron, A.D., Briggs, R.W., Caskey, S.J., Kumar, S., and Owen, L., 2005, Paleoseismic transect across the northern Great Basin: Journal of Geophysical Research: Solid Earth, v. 110, p. 1–25, doi:10.1029/2004JB003283.

Wiedenbeck, M., Allé, P., Corfu, F., Griffin, W.L., Meier, M., Oberli, F., Quadt, A. VON, Roddick, J.C., and Spiegel, W., 1995, Three Natural Zircon Standards for U-Th-Pb, Lu-Hf, Trace Element and Ree Analyses: Geostandards Newsletter, v. 19, p. 1–23, doi:10.1111/j.1751-908X.1995.tb00147.x.

Young, R.A. (Ed.), 1995, The Rietveld Method: Oxford University Press.

Zoback, M.L.C., 1979, A geologic and geophysical investigation of the Beowawe Geothermal Area, North-Central Nevada: Stanford University Publications - Geological Sciences, v. 16.